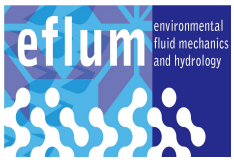

Master of Science in Environment

Stream temperature modeling using fiber optic distributed temperature measurements in a sub-Saharan watershed, Burkina Faso

Author:	**Malik Matthey**, MSc student EPFL
Director:	**Prof. Marc B. Parlange**, EPFL-EFLUM
Supervisors:	**Dr. Hendrik Huwald**, EPFL-EFLUM
	Dr. Alexandre Repetti, Cooperation@EPFL
External expert:	**Prof. Nick v. d. Giesen**, Delft Technical University, Netherlands
External advisor:	**Prof. Scott W. Tyler**, University of Nevada, Reno, USA

June 2010

Abstract

High spatial and temporal resolution water temperature measurements, using DTS, allow to model and to control stream temperature evolution in the Tambarga's basin (Burkina Faso). A wireless sensor network recorded solar radiation, air temperature, air humidity, wind speed (among others) on different sites on Tambarga's basin (B.F.) in 2009. These data, are compiled and used as inputs to force the model and to assess simulated river temperatures in the basin. Local parameters as shade coefficient, stream bed heat losses as well as land coverage coefficient are estimated from "on field" knowledge. Purpose but also need for this study, stream discharge estimation in the Tambarga's river is paramount. Discharges are formed by subsurface flow, groundwater flow and runoff during rain events. Assuming that all three water discharge components have a different thermal signature leads to imagine that they can be identified with the DTS optical fiber, once they reach the main stream. The inflow emplacements are referred to as "springs" in this study. Finally, although this study leads to significant results, the last sections propose the installation of some more measuring instruments for controlling and improving the model accuracy.

La modélisation des températures dans un cours d'eau du bassin versant de la commune de Madjoari (Burkina Faso), est réalisée sur la base de mesures météorologiques à hautes résolutions spatiale et temporelle. Un réseau de stations sans fil mesure la radiation solaire, la température de l'air, l'humidité de l'air ainsi que la vitesse du vent sur le bassin versant près du village de Tambarga et le DTS, installé dans le lit de la rivière, mesure les températures tous les deux mètres et toutes les cinq minutes. Les données ainsi recueillies sont utilisées dans un modèl qui calcule le bilan des flux énergétiques déterminant l'évolution de la température de l'eau dans la rivière de Tambarga et les résultats sont ensuite comparés aux mesures DTS. Les paramètres d'ajustement (ombrage, perte d'énergie dans le lit de la rivière et renvoi de radiation longue par la végétation) sont estimés à partir des connaissances de terrain. La quantification des débits dans le cours d'eau est le but mais aussi un outil nécessaire à ce modèle. Ces débits sont formés par les eaux de ruissellement de surface, des eaux souterraines peu profondes et des eaux de la nappe phrétique plus profonde. L'emplacement des zones de confluences (nommées "springs" dans cette étude) est déterminé à l'aide du DTS étant donné que chacune de ces zones possède une trace thermique différente. Finalement, bien que cette étude mène à des résultats intéressants, les dernières sections de ce document proposent de nouvelles investigations afin d'améliorer la modélisation des températures dans les cours d'eau.

0.1 Acknowledgements

This study is the result of a long process that had been started in spring 2009 by the cooperation@epfl. A two-month internship, made possible by the internship program of the association " Engineer of the World "(IdM), allowed me to familiarize myself with this unknown environment. I would like to thank Alexandre Repetti (Cooperation@epfl) and Lucile Verrot (formerly responsible for internship in IdM).

The first part of this study was conducted in collaboration with the University of Reno with the team led by Scott Tyler that I am grateful for his advise and his welcome in the ("Wolf pack") Nevada state university (USA).

Finally, I want to thank everyone who participated in the various revisions of this study and acquiesced sometimes many hours. Hendrik Huwald, Francisco Suarez, Marc Hausner, Nikki Vercauteren, Natalie Ceperley, Nicolas Volet, Rosa Maria Perea Ibanez, Gian Lieberherr, Murielle Thomet; to all, thank you very much for your support.

Contents

Chapter 1

Introduction

Hydrological resources have always been a limiting factor for livelihoods. When they decrease, all life is endangered, and may die without water. Africa is, among the largest geographic areas of the world where water is a crucial resource for settlement condition. Subsistence, basic needs of population, mine dewatering and infrastructures of urban construction are the main uses of water on this continent. Whereas few papers are available on water management, the Info4Dourou project [3] aims to help the local population managing their resources. It attempts to bring technical and scientific expertise on the subject by bringing together local experts and foreign scientific institutions.
Mainly farming, these populations are highly depending on the amount of rain , its frequency and more generally on water availability. North Africa is one of the main areas subject to water scarcity. Most countries neighboring the Sahara are subject to increased desertification. Although 900 million people live on the continent of Africa and the range of current groundwater issues is tremendous [1], few scientific studies have been published so far on this issue.

To achieve its goals, Info4Dourou scientists have installed (among other actions) a large number of environment sensors in eastern Burkina Faso, near the village of Tambarga. These instruments measure different meteorologic data such as solar radiation, wind speed, air temperature and air humidity (and others). The data used in this study were recorded during summer 2009 . An optical fiber (see figure 2.3), DTS (Distributed Temperature Sensing) has also been used as a new application to measure water temperature along a stream in the studied catchment.

In Tambarga's watershed, many rainfall and temperature data (among other meteorologic measurements) were recorded in 2009 at the rainy season (the summer period). Although high precision instruments were set in the catchment, the water discharge gage did not record any data, or not reliably. The final goal of this study is to attempt to assess these discharge series in time by simulation. The method used to get this simulation will be described later on.

The way to derive this discharge is to use an energy balance along with a water mass balance on each sub-basin. Starting from the upper region of the catchment, the temperature is computed according to a first order upwind scheme [24]. Modeled stream temperatures are compared to those measured with the optical fiber. Furthermore, DTS measurements accuracy were assessed in some places with tiny temperature loggers (Tidbits; single point temperature measurements in time) at points of confluence.

Water temperature in the river can be linked to water discharge as long as we can model precisely all components of the energy balance acting on each water drop within the stream at any time. In this basin, stream water flow is calculated by adding rainfall water and surface water to groundwater flow as shown in scheme 1.1, [23]. A thermal signature allows to differentiate them with the DTS stream temperature sensor (see figure 2.4). If we know the inlets' temperature and the energy balance acting in space at any time on a reach of the river, we are able to predict water temperature's behavior all along the stream for a given discharge. **Unfortunately, no data can confirm the modeled discharges**.

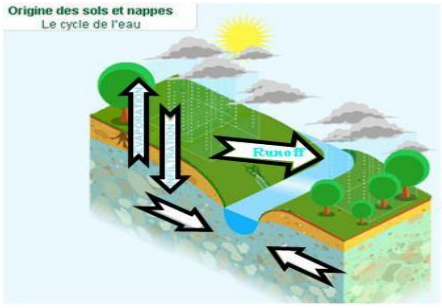

Figure 1.1: **Water's sources and sinks around the main stream**

The energy balance is calculated on the basis of meteorologic data measurements. Next chapter explains the type of measurements and how they were installed on the basin.

Chapter 2

Measurement systems

To model the energy balance of the stream, this study uses data collected during summer 2009 by two energy balance ("Eddy correlation") stations (MET[1] [8] see figure 2.1) and several sensorscope stations [9] (SSC). The stations are set on the field (see figure 2.8) and are equipped with various sensors.

Figure 2.1: **Energy balance (EB) station. This station is located on a hill**

The two EB stations (MET) measure all components necessary to compute heat fluxes balance. One was installed on a plateau avove the valley and the other one on the plain (see figure 2.2). These two stations are complemented by stations in others locations of the catchment. This increases the spatial resolution of meteorological measurements. However, within or on the stream bed, goal of this study, only DTS and some tidbits have collected data. As none of the meteorological sensors was located on the stream, some hypotheses are necessary to calculate the energy balance from the land and to translate it on the stream. Shadow effects C_s as well as riparian vegetation and land cover θ_{VTS} influences are introduced in the stream temperature model and estimated by these parameters.

[1] Meteorological station

2.1 Energy balance

In order to model water temperature evolution in space and time, we need to know the amount of energy reaching and leaving the stream at anytime and any place along the river. The balance of these energy fluxes (coming in and out) will then be used to calculate water temperature. This balance shall take into account solar radiation and long wave radiation (mainly inputs), as well as latent evaporation, sensible heat and ground energy flux (mainly outputs). Such a balance is given by [2](Brutsaert, 2005) and is used in this study as in equation 2.1.

$$\frac{\partial W}{\partial t} = R_n - L_e E - H + L_p F_p - G + A_h \tag{2.1}$$

R_n is the net radiation flux density at stream water surface, L_e is the latent heat of vaporization, E is the evaporation, H is the sensible heat flux, L_p is the thermal conversion factor for carbon dioxide fixation, F_p is the specific flux of CO_2, G is the specific energy flux leaving the stream through the bed (lower boundary layer), A_h is the energy advection into or out of the stream and $\frac{\partial W}{\partial t}$ is the rate of energy storage per unit horizontal area $[W/m^2]$.

In this study, as we are not considering a soil, but a river, and as we did not directly measure all these parameters, we solve the equation 2.2 to determine the residual energy.

$$R_n - L_e E - H - G = Residual \tag{2.2}$$

The "Residual" term contains all **the energy stored in water** while flowing, the energy interception from riparian vegetation and the eventual advection sink/source acting on the stream.

2.2 Instrument description

As the model relies on sensor technologies applied in the environment, this section describes the different devices that were used. All data used here are available from the web [9]. A data storage system (memory card), powered by a solar panel, has a memory that allows a nearly 10 days autonomy. For this reason some data sets have some gaps at some stations because memory cards could not be changed.

Data from station MET 2 (see figure 2.2), located in the middle of the basin, were used in this study as input to model stream temperatures. The main reason for this is that all the sensors necessary to run the model had complete data records only on this station.

Sensorscope station

"SensorScope is a new generation of measurement system based on a wireless sensor network with built-in capacity to produce high temporal and spatial density measures. By gathering the most recent results from a large range of research domains, we aim at providing the fundamental tools that will help in taking care of our environment." [10]

Air temperature

Measured 1.5 [m] above the surface, at one minute time interval with a humidity and temperature sensor (SHT).

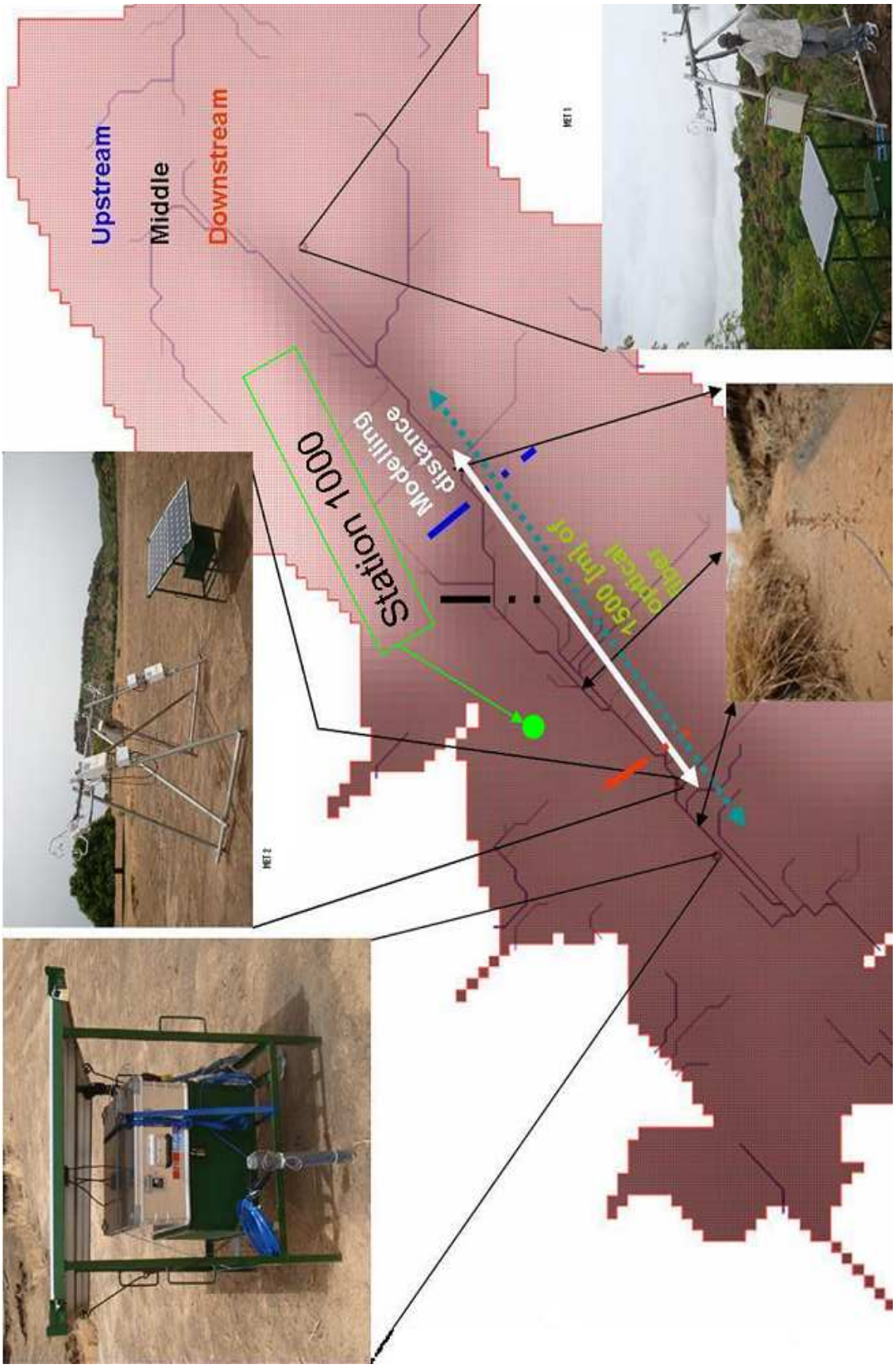

Figure 2.2: **Instruments location in the catchment, modeling domain and points of data analysis (Upstream, middle and downstream)**

Air humidity

Measured above the surface, at one minute interval with a SHT sensor.

Solar radiation

The global incoming radiation (short-wave (SW) and long-wave (LW)) is measured with "Davis instrument pyranometers" sensors. Data are recorded every thirty seconds. The sensor is located (2 m high) on the top of the station (see figure 2.1). The point of measurement is ten meters away from the stream, and the surrounding conditions (mainly shadow, direct and indirect light) are not identical to the station near the stream surface. However, the study assumes that parameters, if well calibrated, can correct for these differences.

Wind speed

Measured 2 [m] above the surface, at thirty seconds time step with a "Davis instrument pyranometer"

DTS optical fiber

Figure 2.3: **Start of DTS in the valley (see figure 2.2). The blue coil of the optical fiber is visible.**

The DTS optical fiber has been installed in the stream bed of Tambarga's river. The length of the fiber is 1,500 [m] simple way. When the river has a water flow, the optical fiber measure it's temperature at the outside interface between the cable et the water. The spatial resolution of measurement is 2 [m], the frequency is 5 [min] and the accuracy ranges from 0.01 to 0.5 °C (see [21] and [3]. The optical fiber inside the cable is double ended. The light inside the fiber move along the length in both ways. In the whole, the beam travels 2*1,500 [m] inside the cable. One calibration coil checked by thermometers allow to correct for a possible offset and drift along the fiber. Using an optical fiber for field measurements has two main practical advantages:

◦ Measure the stream temperatures **continuously** using nothing but the optical fiber properties.
◦ Do not disturb the environment in which the device is installed. We have to calibrate it as mentioned above.

DTS physical principle:

◦ Optic fiber acts as a thermometer with a laser as light source.
◦ Rayleigh, Raman and Brillouin dispersions occur all along the way of light in the optic fiber (see figure 2.5).
◦ Raman diffusion is due to inelastic collisions of photons with molecules within the fiber. When a photon "gives" energy to the fiber, its wave length disperses (Stokes signal). When a photon "gains" energy, its wave length becomes shorter (anti-Stokes signal).
◦ Raman spectra is foreseeable and symmetric.

◦ Anti-Stokes (gained energy) are strongly temperature dependent whereas Stokes are independent of temperature met at collision points.
◦ Temperature at collision points is calculated according to the ratio of the anti-Stokes to Stokes peaks (see figure 2.5)
◦ As installed here, a solar panel and a battery power the instrument

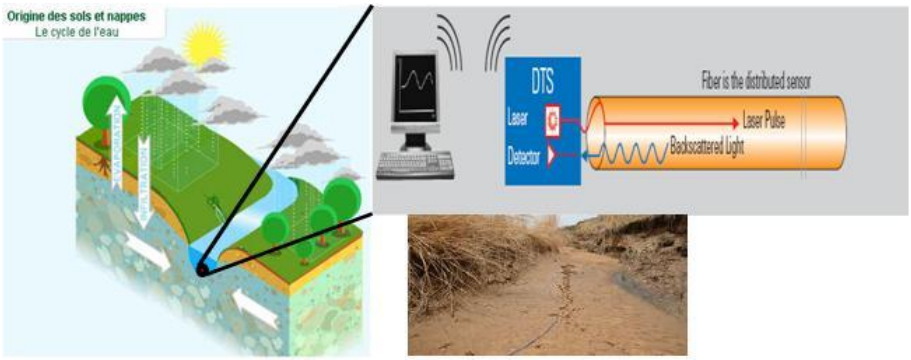

Figure 2.4: **DTS optical fiber deployment. The optical fiber has been installed on a 1,500m reach within Tambarga's riverbed [23].**

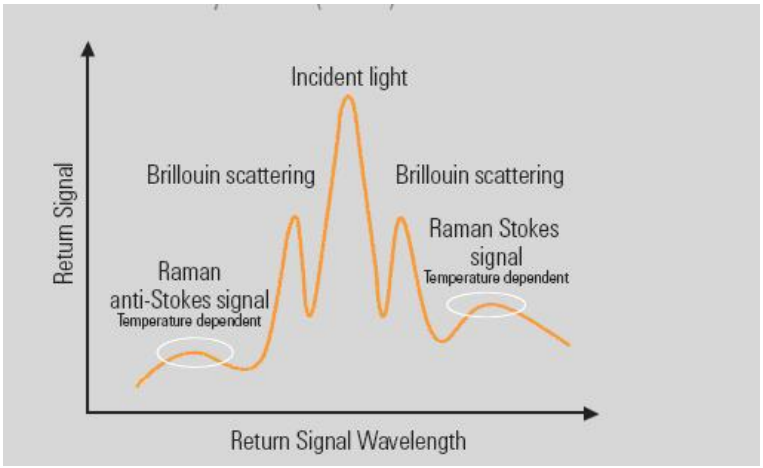

Figure 2.5: **Raman spectra**

Tidbits

In some places along the main river, temperature data loggers (see figure 2.6) were buried in the stream bed at confluence points. The diameter is about 30 [mm]. One of them was also installed in the DTS calibration coil. It gave consistent data and permitted to check DTS data accuracy. It has also confirmed that temperatures measured with the optical fiber present no evident drift along the cable as shown in figure 2.7.

Figure 2.6: **Temperature data logger at real size**

Figure 2.7 illustrates the agreement between Tidbit and DTS measurements for the same time period and at the same place. DTS temperature is averaged over the length of the calibration coil for both directions. We can see in figure 2.7 that the temperature difference between Tidbit and DTS cable measurements, is near 0.2 °C at maximum. The time shift in temperature series (between tidbit and DTS) is due to response lag of the tidbit as a result of the low conductive material of the instrument.

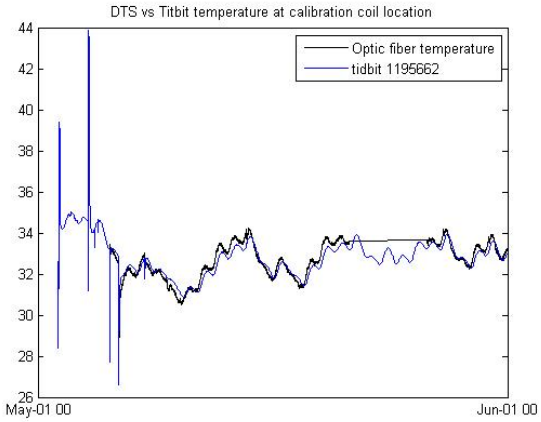

Figure 2.7: **Tidbit temperature compared to DTS temperature measurements averaged over the length of the calibration coil**

Rain gage

Installed in the field on sensorscope stations, this gage measures the intensity and amount of rainfall events. At the beginning of the rainy season, the gage measure the “true” rainfall. Yet, as we move forward into the rainy season, vegetation might bias a little the measurements.

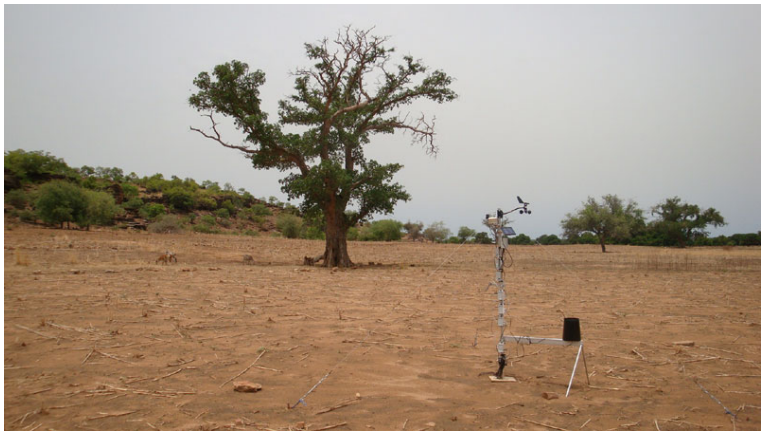

Figure 2.8: **Sensorscope station with a rain gage. Sandy soil surface creates high runoff rates**

Chapter 3

Stream temperature model

As we don't have any discharge measurement at any place along Tambarga's stream, the model assumes, in a first attempt, a constant discharge coming out of a single source upstream even though two springs had been previously identified [13]. Finally, a small discharge (roughly estimated at 20 [l/s]), a shallow depth of water and a slow velocity assume that a part of the incoming radiation is absorbed by the stream bed. The fraction of the incoming radiation reaching the stream bed is called D_f in this study. Once we obtain accurate results, we increase the complexity of the model up to the highest level where we'll include subsurface and groundwater inflow into the main river. This study applies an approach proposed in a previous study ([24]) on a river in the Netherlands. The river is divided in many reaches on which the complete energy budget will be calculated using sensorscope data. The energetic fluxes on every segment are shown schematically in figure 3.1.

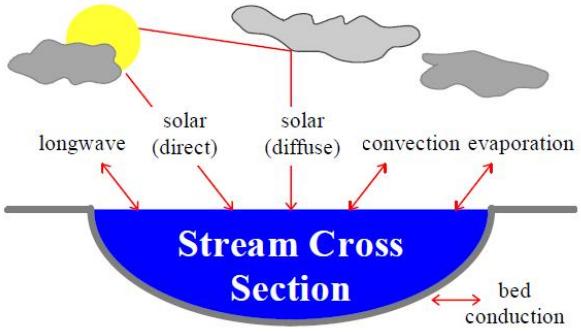

Figure 3.1: **Energy fluxes acting on the stream boundaries [22]**

As a large amount of energy is also stored into the flowing water, this energy budget has to take into account an advection term. This term is not shown in figure 3.1 but appears in figure 3.2. Moreover, within a segment-volume, we assume a total mixing and therefore a constant temperature inside each segment. For this reason the dispersion term inside a section is insignificant.

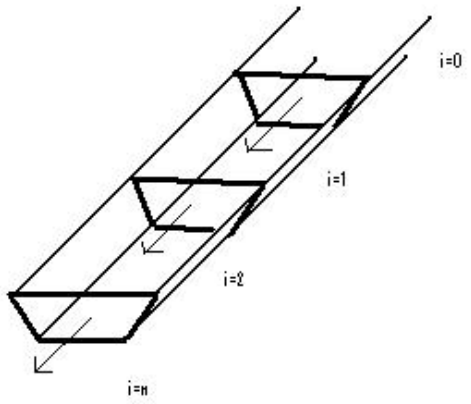

Figure 3.2: **Channel with spatial discretization to illustrate equation 3.10**

3.1 Mathematic expression of the model

The governing equation used in the model is the following:

$$\frac{\partial A}{\partial t} + \frac{\partial Q}{\partial x} = q_L, \tag{3.1}$$

Where A is the stream cross section, Q is the discharge in the stream and q_L is a specific inflow discharge from a tributary into the main river. The mass conservation equation 3.1 guaranties that for each node, the amount of water flowing out corresponds to the sum of inflows. For the energetic balance we have:

$$\frac{\partial (AT)}{\partial t} + \frac{\partial (QT)}{\partial x} = q_L T_L + R, \tag{3.2}$$

Where T is the water temperature and R is the sink/source term [24] and is calculated as follows;

$$R = \frac{B\phi_{total}}{\rho_w c_w}. \tag{3.3}$$

The net energy exchange (see figure 3.1), on each segment of the stream, appear in equation 3.3 as ϕ_{total} in [W/m^2]. In finite volumes, a finite difference scheme for equations 3.1 and 3.2 can be written as follow:

$$\frac{dV_i}{dt} = Q_{i-\frac{1}{2}} - Q_{i+\frac{1}{2}} + Q_L \tag{3.4}$$

$$\frac{dV_i T_i}{dt} = Q_{i-\frac{1}{2}} T_{i-\frac{1}{2}} - Q_{i+\frac{1}{2}} T_{i+\frac{1}{2}} + Q_L T_L + \frac{R_i V_i}{A_i} \tag{3.5}$$

Where "i" is the spatial index, $i-\frac{1}{2}$ and $i+\frac{1}{2}$ indicate the upstream part and downstream part of segment "i" respectively for temperature and discharge. As we assumed that no dispersion is taking place within a cell, and that temperature is constant in this volume, we calculate temperature evolution at an imaginary middle point between two segments (see equations 3.4 and 3.5). These two temperatures are defined as follow;

$$T_{i-\frac{1}{2}} = T_{i-1} + \Delta T_{i-1} \tag{3.6}$$

$$T_{i+\frac{1}{2}} = T_i + \Delta T_i \tag{3.7}$$

and

$$\Delta T_{i-1} = \frac{max(0, \Delta^+ T_{i-1} \Delta^- T_{i-1})}{T_{i-1} + T_{i-1}} \tag{3.8}$$

$$\Delta T_i = \frac{max(0, \Delta^+ T_i \Delta^- T_i)}{T_i + T_i} \tag{3.9}$$

Schematically, these temperature gradients between two segments can be drawn like in figure 3.3.

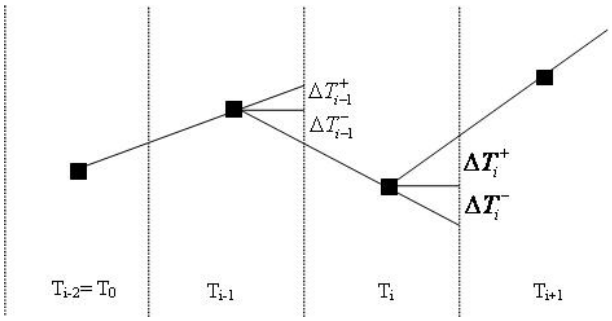

Figure 3.3: **Illustration of "Van Leer limiters" used to compute temperature in different segments [24]**

Finally, the upwind temperature model, from equation 3.5 can be re-written as in equation 3.10

$$\frac{dT_i}{dt} = \frac{Q_{i-\frac{1}{2}}(T_{i-1} - T_i)}{V_i} + \frac{Q_{i-\frac{1}{2}} \Delta T_{i-1} - Q_{i+\frac{1}{2}} \Delta T_i}{V_i} + \frac{Q_L(T_L - T_i)}{V_i} + \frac{R_i}{A_i} \tag{3.10}$$

The first term on the right hand side is a first order upwind, and the second is an anti-diffusion term. Temperature gradient is done with a Lax-Wendroff type of time integration [24].

3.2 Nummerical scheme of temperature model

Starting with equation 3.10, temperature prediction is done as follows;

$$\frac{T_i^{n+\frac{\Delta t}{2}} - \frac{T_{i-1}^{n-1} + T_{i-1}^n}{2}}{\frac{1}{2}\Delta t} = \frac{Q}{V}\Big((T_{i-1}^n - T_i^n) + (\Delta T_{i-1}^{n-1} - \Delta T_i^{n-1})\Big) + \frac{R_i^n}{A} \tag{3.11}$$

The Lax-Wendroff type of time integration is introduced on the left hand side. We can schematically illustrate the calculation of equation 3.11 as in figure 3.4 with the left term in orange arrow, and the right terms in blue arrows. The time index, n, depends on the duration of the simulation

$$T_i^{n+\frac{\Delta t}{2}} = \frac{T_{i-1}^{n-1} + T_{i-1}^n}{2} + \frac{1}{2}\Delta t\left(\frac{Q}{V}\Big((T_{i-1}^n - T_i^n) + (\Delta T_{i-1}^{n-1} - \Delta T_i^{n-1})\Big) + \frac{R_i^n}{A}\right) \tag{3.12}$$

The linear equation 3.11 can be written in a matrix form. Solving for $T_i^{n+\frac{\Delta t}{2}}$ and T_i^n at a given time $n + \frac{\Delta t}{2}$ and for all the "i" spatial sections, we obtain:

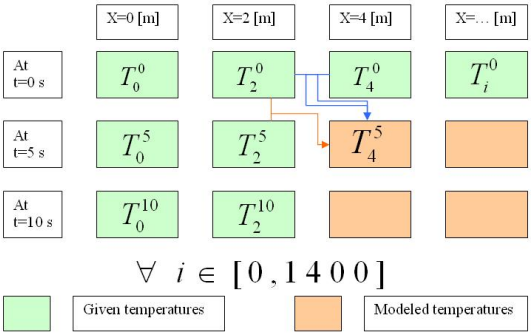

Figure 3.4: **First order upwind finite difference scheme**

$$\overrightarrow{y} = A\overrightarrow{x} + \overrightarrow{b} \tag{3.13}$$

$$\mathbf{A} = \frac{Q}{V}\begin{pmatrix} a_{11} & a_{12} & \dots & a_{1i} \\ a_{21} & a_{22} & \dots & a_{2i} \\ \vdots & \vdots & \ddots & \vdots \\ a_{i1} & a_{i2} & \dots & a_{ii} \end{pmatrix} = \frac{Q}{V}\begin{pmatrix} -1 & 0 & \dots & 0 \\ 1 & -1 & \dots & 0 \\ \vdots & \vdots & \ddots & \vdots \\ 0 & \dots & 1 & -1 \end{pmatrix}$$

$\overrightarrow{y}$ represents the left term of equation 3.11. $\overrightarrow{x}$ is the temperature vector at time "n" for all the distances "i". $\overrightarrow{b}$ contains the energy balance and the temperature limiters. Inverting A gives;

$$\overrightarrow{x} = A^{-1}\left(\overrightarrow{y} - \overrightarrow{b}\right) \tag{3.14}$$

3.3 Simulation hypothesis

The Madjoari's catchment is divided in 600 small zones of two (2) meters each located on the stream. With a length of 2 [m], a width of 0.4 [m] and a depth of 0.07 [m], the volume of each cell is 0.056 $[m^2]$ and the energy exchange area is 0.8 $[m^2]$ It allows calculating a relevant average temperature (of DTS data) inside water and also provides an accurate standard deviation on these water temperatures. The time step used for simulations is given in equation 3.15.

$$\frac{V_{cells}}{Q} = \frac{WidthDepthLength}{Q} = \frac{0.056}{0.02} = 2.8[s] \tag{3.15}$$

The average river flow velocity, v (estimated from manual measurements [11]) is about 0.7 [m/s]. This value is conserved by the above equation 3.15. Within this time, and for each section, the net energy will be computed and added in order to simulate the temperature evolution all along the optical fiber.

To start with temperature modeling in the stream, we assume in a first step that the discharge downstream from "source 2" (see figure 3.5) is equal to the one downstream under the bridge (downstream on the river), with a constant cross section area and therefore the temperature evolution is calculated always on a constant volume. At this state there are no other springs but "source 2" along the river adding water into the main river. Later, we will add a second entry of water at "source droite" assessing the discharge and temperature of this lateral inflow. Figure 5.1 and following show temperature evolution along the DTS for different periods during the rainy season.

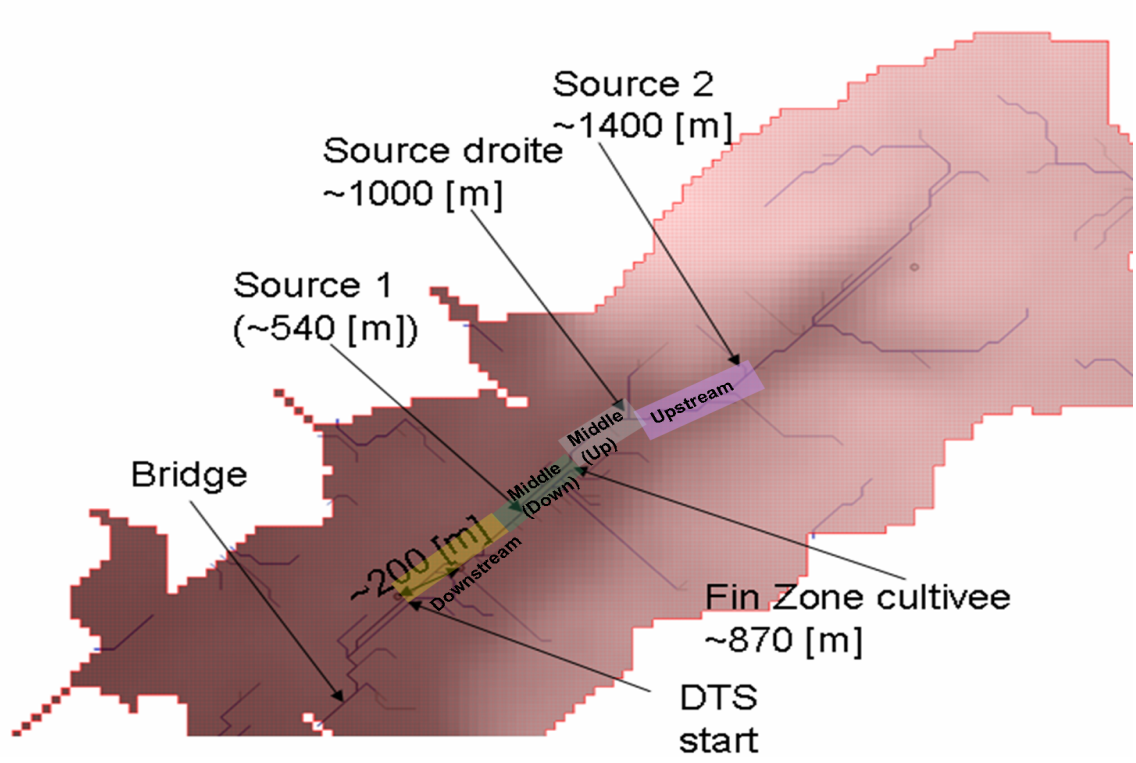

Figure 3.5: **Springs in the tambarga catchment**

"Atmospheric variables" are measured. None of the hydrological parameters are available. As a first guess, we take a constant section area of flow and a discharge of 20[l/s]. All the riparian parameters are estimated. Although, vegetation changes during the wet season (June to September), we keep them constant. The temperature inputs are measured with the DTS. For the **"Heat energy processes"** only the solar radiation is measured. Evaporation, convection and long-wave fluxes are computed using the model of M.C. Westhoff et al. [24]. **Temperature prediction** uses advection terms, limited dispersion (Van Leer limiters) no groundwater mixing until middle of July and a heat energy balance.

Figure 3.6 displays the structure and scheme of the model with all its individual sections and processes. The following section explains how observational data are used as inputs to force the model in the Tambarga river.

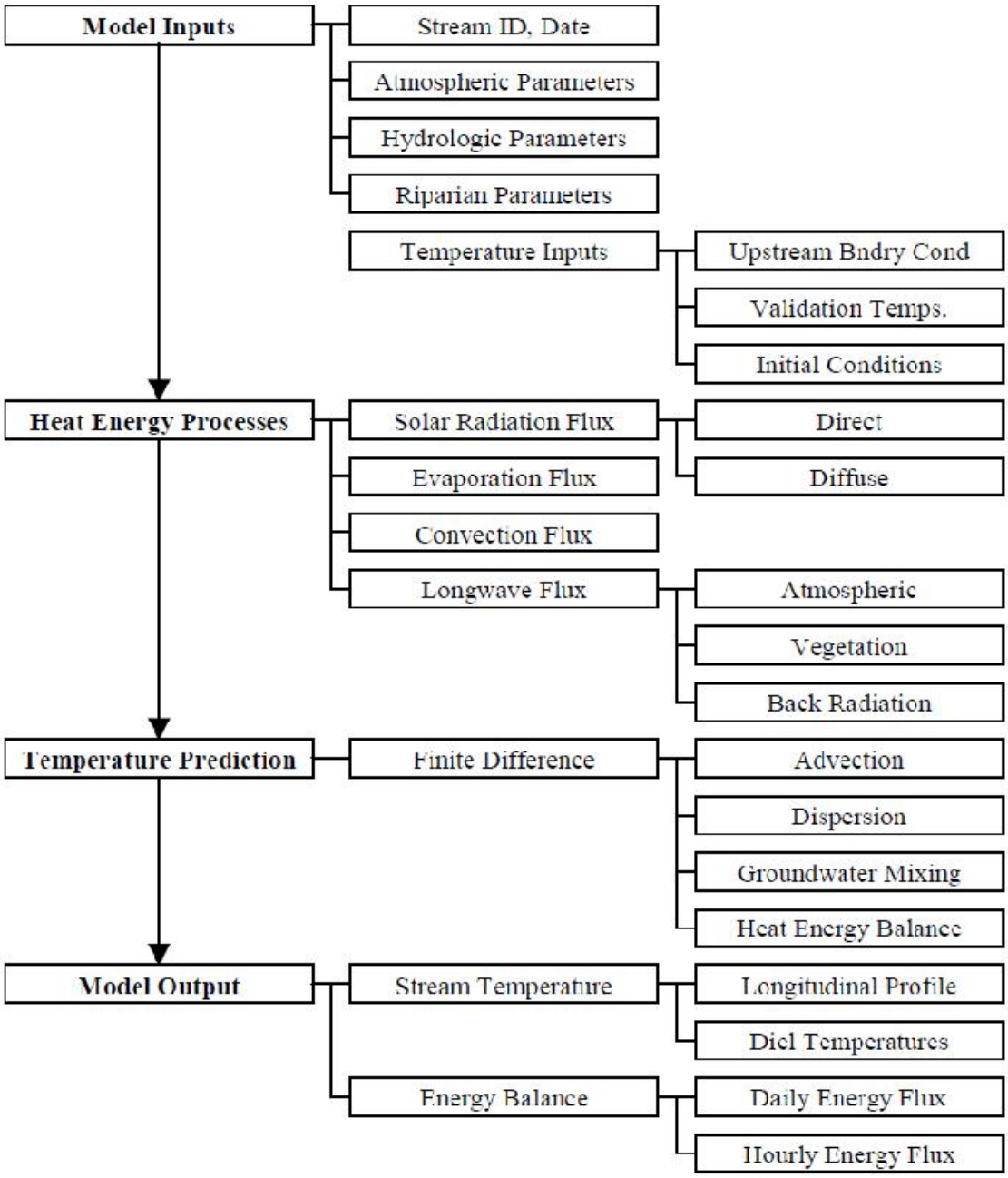

Figure 3.6: **Schematic of a stream temperature model and its forcing variables [22]**

Chapter 4

Model input variables

Stream temperature modeling depends on a large amount of input data. These data must be accurate, compatible and available in a resolution fine enough to allow comparisons with reality. We first need to define the part of the stream where the model will be implemented. When no relevant data are available, we are forced to make a hypothesis. For stream temperature, solar radiation is the main factors for water temperature variation in a day. Although this model uses the global solar radiation as main input data, these latter were adjusted using parameters from land measurement to "on stream" application. The parameters that were determined for the condition the original study of Westhoff et al. ([24]) have to be validated and possibly changed in order to use them in soudanian conditions like in Burkina Faso. This is the aim of the following section.

4.1 Atmospheric variables

Air emissivity

The atmospheric emissivity, ϵ_{atm}[-], hasn't been measured on-site in Burkina Faso. Following Westhoff et al. [24], this parameter can be calculated (see equation 4.1) with the Brunt coefficient, B_c [-],an empirical constant α_1 $[kPa^{-0.5}]$ and the current vapor pressure e_a [kPa]. The latter can be determined from relative humidity measurements.

$$\epsilon_{atm} = 1.1B_c + \alpha_1\sqrt{e_a}, \tag{4.1}$$

with

$$e_a = \frac{H_r}{100}e_s, \tag{4.2}$$

H_r is the relative humidity and e_s is the saturation vapor pressure at a given temperature:

$$e_s = 0.61275exp^{\left(\frac{17.27T_{air}}{237.3+T_{air}}\right)} \tag{4.3}$$

Another way to calculate the vapor saturation curve [2] gives similar results for the temperature range of the study (between 25 and 35 °C) as we can see in figure 4.1. Air relative humidity, H_r, has been measured on site as well as air temperature, T_{air}.

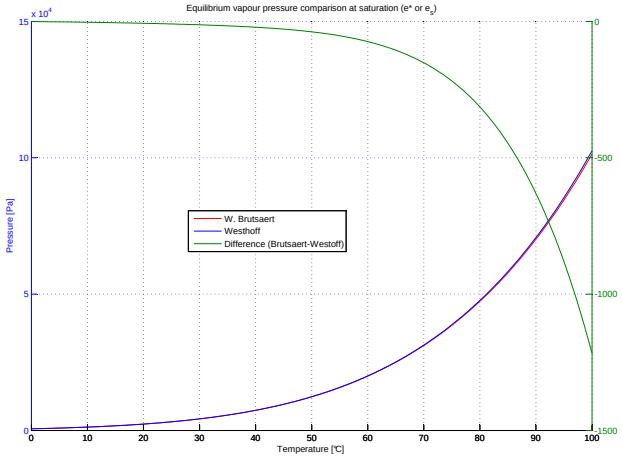

Figure 4.1: **Comparison of saturation vapor pressure according to the model used in Westhoff ([24]) and in Brutsaert ([2]). At 35 °C, we have a difference of -20[Pa].**

Pressure

The barometric air pressure, p_A [kPa] is calculated for a given altitude, z, with the equation 4.4 [24].

$$p_A = 101.3 + 0.01055z \tag{4.4}$$

In the related region in Burkina Faso, the altitude varies from 210 [m.s.l.] to 320 [m.s.l.][1]. As the highest point (320 [m.s.l]) has not any water, we can assume as a rough approximation that the altitude **z=220** [m.s.l.] in average is the elevation of the river where simulations will take place.

Air physical properties

The Bowen ratio, B_r is computed [24] as in equation 4.5. It represents the ratio of sensible heat flux to evaporation.

$$B_r = 6.110^{-4} p_A \frac{T - T_{air}}{e_s^w - e_a^w} \tag{4.5}$$

Where T is the water temperature, e_s^w and e_a^w are respectively the saturated and actual vapor pressure using the stream temperature.

With these parameters, we are able to calculate energy fluxes such as long-wave radiation from the atmosphere, evaporation and latent heat flux. To quantify the solar energy coming into the main river, we need to define the riparian coefficients along the stream. This is done in the following section.

[1] Meters above sea level

4.2 Riparian and ground variables

Tambarga's basin can be divided into three parts; The canyon, the upper plain and the lower plain. The upper plain is divided in two parts depending on sun irradiation (see figure 3.5). This makes the "shadow" (C_s) and "view to sky" (θ_{VTS}) coefficient to vary. "Upstream" zone is covered with a forest and some riparian vegetation. Middle "up" zone has still some trees, but they are spread over the area, whereas "middle down" part has no trees anymore and only riparian vegetation. Finally, "downstream" part is a steep little ravine with a lot of shade.

Parameters are taken to be constant in time but not in space (see table 4.1). Although vegetation changes during the rainy season, these parameters do not change. It can be true that conditions are not changing in the canyon (upstream part), but it's wrong for other parts. Nevertheless, the interest in keeping them constant is that we might see the effect of crops in areas surrounding the river on stream modeled temperatures.

The next sections explain why now values have been assigned to these parameters. It also discusses how relevant these values are.

Stream bed energy flux, D_f

As shown in equation 4.6, D_f represents the amount of solar radiation directly reaching the stream bed without warming water. Although we assume a constant discharge all along the studied reach of the river, we use this parameter to show the water depth's influence on the energy reaching the bed. That is why, upstream, D_f=0.4 and decreases to D_f=0.3 downstream.

Shadow effect, C_s

$$\phi_{solar} = C_s(1 - D_f)\phi_{global} \tag{4.6}$$

ϕ_{solar} $[W/m^2]$ is the short wave (SW) solar radiation flux reaching the catchment (the smaller the shade coefficient, the higher the rate of shade). ϕ_{global} is measured by a "Davis" solar radiation system installed on station 1000 (see figure 2.2). As water is flowing through a "spread forest" (most upstream part, see **??**), the incoming light is reduced by 30 % (C_s=0.7). The transition between the canyon and the plain is smooth however, an important temperature elevation was noticed (C_s=0.95). Further downstream, it goes through a crop area with riparian vegetation at the river sides (C_s=0.6) to end up in an eroded section with steep banks (C_s=0.3).

"Land cover" influences, θ_{VTS}

Long-wave radiation from the atmosphere to the river is modified due to riverside vegetation expressed in the "view to sky" (ϕ_{VTS}) coefficient. Infra-red radiation is absorbed by vegetation. The higher the covering rate is, the smaller is the amount of long-wave radiation reaching the stream bed. This is considered in equation 4.7 by the factor θ_{VTS} which is missing in Westhoffs original equation.

$$\phi_{atm} = 0.96\epsilon_{atm}\theta_{VTS}\sigma_{sb}(T_{air} + 273.2)^4 \tag{4.7}$$

ϵ_{atm} is the emissivity of the air (see equation 4.1) and σ_{sb} is the Stefan-Boltzmann constant ($5.67{*}10^{-8}[W/(Km^2)]$).

On the other hand, surface emitted long-wave radiation cooling the river depends on the "Black body" emission process. The stream is considered as an almost black body which emits long wave radiation into the atmosphere.

Coupled with long wave coming from the atmosphere, some of this radiation will enter into the near-stream vegetation. This latter warms up during the day, and releases energy during the night. The land cover proportion along the stream has a linear relation with the amount of energy sent back to the stream. Riparian vegetation will have a "green house" effect and therefore, will prevent a certain amount of energy losses from the river by long-wave radiation.

$$\phi_{landcover} = 0.96(1 - \theta_{VTS})0.96\sigma_{sb}(T_{air} + 273.2)^4 \tag{4.8}$$

Land cover changes as the rain season progresses. However, parameters are taken to be constant. This will discussed in more details later on. "View to sky" coefficient is nearly constant except in the downstream part of the river where it decreases considerably to take into account the effect of steep banks. In most of the upstream part, water flows in a forest where 60 % of energy is captured by trees (θ_{VTS}=0.4) and after, on the plain, riparian vegetation and crop increase the incoming energy to 50 % (θ_{VTS}=0.5).

Summary

Parameters	$Upstream$	$Middle(up)$	$Middle(down)$	$Downstream$
C_s	0.70	0.95	0.6	0.30
θ_{VTS}	0.4	0.5	0.5	0.2
D_f	0.40	0.40	0.30	0.30

Table 4.1: Coefficients for shadow (C_s), sky view (θ_{VTS}) and stream bed energy conduction (D_f) into the deeper alluvium

As shown in figure **??**, the basin is divided in four areas subject to different regimes of solar radiation. In the upper part, the river flows in a sparse forest with an increasing riparian component as we get into the rainy season. In the middle section, we enter an "open-flow" zone that progressively becomes riparian with the rainy season. At last, in the lower part, the river flows in a deep (2 m) channel and for this reason, solar radiation is limited (except maybe at noon time).

At this stage, it would be very convenient to use a GIS map in order to give more accurate values to these coefficients. It would allow calculation of the energy balance with a higher accuracy and it would also improve the model representativity. As we don't have any measurements nor precise enough maps, we have to proceed, with the current knowledge and these rough estimations.

4.3 Hydrologic variables

Normal discharge

Though discharge gage did not work during the summer 2009, some manual heights of water measurements were made. Below the bridge (see figure 3.5), water velocities were measured. As we have all the geometric characteristics of the channel under the bridge (width, length, slope and average grain size), we can estimate a discharge, Q, according to Manning-Strickler [14].

$$Q = Av = AK_s R_h^{\frac{2}{3}} J^{\frac{1}{2}} [m^3/s] \tag{4.9}$$

$$K_s = \frac{21.1}{\sqrt[6]{d_{50}}} \quad [m^{\frac{1}{3}}/s] \tag{4.10}$$

Where A is the cross section area of flow, υ is the stream water velocity according to Strickler, R_h is the hydraulic radius and J is the slope. Strickler roughness coefficient depends on the average grain size in the river. It was admitted that d_{50}=0.002 [m] and K_s=59.4 $[m^{\frac{1}{3}}/s]$. For the days when we collected measurements we obtain the discharges that are shown in figure 4.2. At the beginning of July, stream water discharge at the bridge (measurement point, see figure 3.5) is about 0.02 $[m^3/s]$. This discharge will be used for the first simulations.

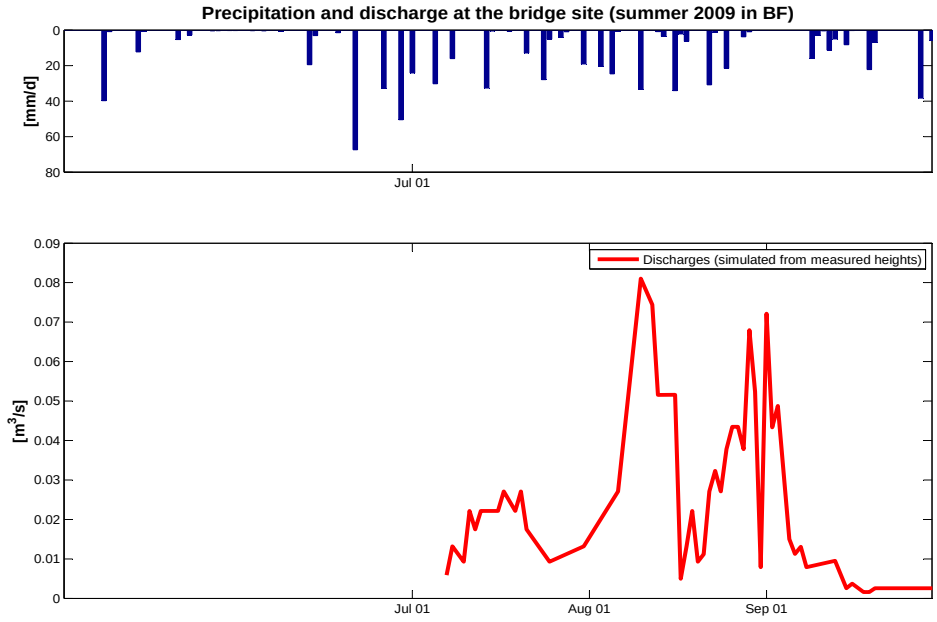

Figure 4.2: **Precipitation and discharge estimated from manual measurements**

Naturally we model a single upstream inflow bringing water at a constant discharge of 20 [l/s]. The channel geometry is constant all along the length of modeling domain. Stream temperature, at each section, only depends on upstream section water temperature and energy balance at a given time. Figure 6.1 shows schematically that groundwater and subsurface water do not affect stream temperature under certain conditions.

Discharge during rainfall

To assess the temperature evolution, the sensibility to rain events, and the effect of springs, we choose here three dates at the beginning of the wet season. These dates appear in bold in table 4.2. They correspond to the highest (amount and/or intensity) rain events. At these times, we compared DTS stream temperature profiles. As these floods took place at the beginning of the rainy season, they were mainly transformed into runoff as no intercepting and harvesting plants could prevent it (see figure 2.8).

Rain events are usually of high intensity at the beginning which decreases in time. Except for June the 29th when the rainfall event lasted for many hours. For this reason, stream temperature profiles evolve smoothly as we will see in the following section.

Assuming a constant slope for the runoff, a constant runoff coefficient C_R and a semi-circular area A, we can use equation 4.11 to estimate the discharge in the river during a rain event of intensity "I" [mm/h].

Dates	$Start(Hour)$	$End(Hour)$	$Duration[h]$	$Amount[mm]$	$Intensities[mm/h]$
08/05/09	02:00:22:90	05:39:48:50	02:39	39.8	15.02
14/05/09	19:01:34:10	19:49:22:20	00:48	12.3	15.38
13-14/06/09	22:51:08:20	02:55:16:50	04:05	22.6	5.53
21/06/09	**00:09:28:10**	**08:28:47:20**	**08:19**	**67.4**	**8.16**
26/06/09	09:54:37:40	14:11:12:50	04:17	32.8	7.66
29/06/09	**10:36:29:20**	**11:34:37:30**	**00:58**	**50.5**	**52.24**
01/07/09	00:24:24:80	04:35:59:80	04:11	24.2	5.78
05/07/09	07:37:07:90	10:42:28:40	03:05	30.3	9.83
08/07/09	02:20:01:50	02:54:06:60	00:34	16.1	28.41
14/07/09	03:08:08:50	08:03:25:60	04:55	32.7	6.65
21/07/09	01:44:56:50	07:42:46:60	05:58	12.9	2.16
24-25/07/09	**22:27:04:00**	**03:35:25:10**	**05:08**	**33.1**	**6.44**
27/07/09	05:55:46:00	12:23:23:50	06:28	4.1	0.63
31/07/09	03:55:12:50	09:07:45:50	05:12	19.1	3.67
03/08/09	02:26:30:50	13:41:22:30	10:45	20.4	1.89
05/08/09	21:30:17:80	23:59:37:00	02:29	24.7	9.95
10/08/09	03:25:03:30	08:23:36:10	04:58	33.4	6.72
14/08/09	21:38:37:60	21:52:50:10	00:14	3.6	15.43
16/08/09	08:48:56:40	11:09:21:70	02:21	34.1	14.51
22/08/09	17:41:20:10	23:39:55:70	05:58	30.9	5.18
25/08/09	01:53:19:80	08:09:26:00	06:16	21.6	3.45
28-29/08/09	19:49:20:20	01:27:39:30	05:38	4.8	0.85
09/09/09	11:36:04:00	22:07:19:30	10:31	15.9	1.51
10/09/09	21:11:09:20	23:26:58:80	02:15	2.9	1.29
12/09/09	03:38:39:80	06:55:33:80	03:17	11.4	3.47
19-20/09/09	22:34:14:80	04:09:38:00	05:35	29.2	5.23
28/09/09	03:55:12:90	04:56:19:90	01:10	38.3	32.83
30/09/09	17:20:08:30	19:13:11:10	01:53	5.8	3.08
11/10/09	18:24:51:70	19:04:02:60	00:40	12.9	19.35
12/10/09	21:00:35:60	22:23:21:70	01:23	26.5	19.16

Table 4.2: Rain periods during summer 2009 on Tambarga's watershed. Bold lines identify events used in the data analysis

$$Q = C_R I A [\frac{m^3}{s}] \tag{4.11}$$

Working with a digital elevation model (DEM) of Tambarga's region, we can draw the water channel on the basin and estimate the area of flow to reach a given output (see figure 4.3).

Zones	*Upstream*	*Middle*	*Downstream*
C_R	0.6	0.6	0.4
I [mm/h]	20-50	20-50	20-50
A $[km^2]$	0.27	0.21	0.13
Q $[m^3/s]$	**0.9-2.25**	**0.7-1.75**	**0.29-0.72**

Table 4.3: Estimation of discharges in the river for a range of rainfall intensities using equation 4.11

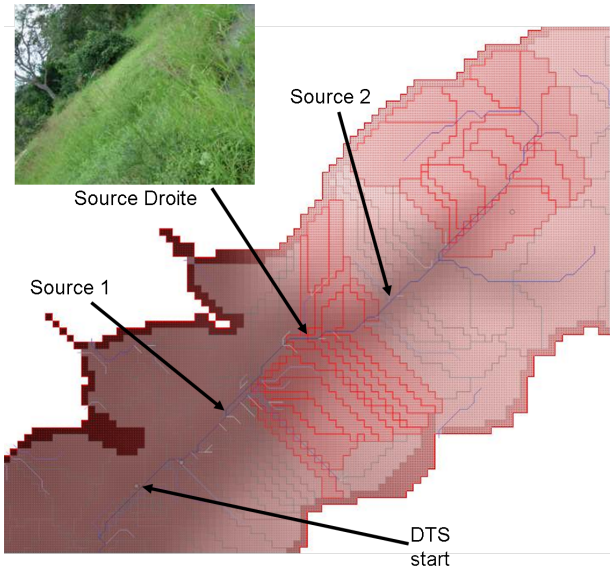

Figure 4.3: Map of the modeled tributaries drainage areas

The areas that feed the stream are in evidence (in red). Table 4.3 presents the assumptions (personal communication[2]) made for the runoff coefficients of the different areas. The rain intensities are taken from table 4.2.

During rainfalls, the river discharge can increase considerably to reach a maximum value of 4.72 $[m^3/s]$ (if we sum all maximum discharges from table 4.3). Again, at that point, we do not have any discharge measurement downstream of the river to confirm this value. Also, as some rain events have a long duration, the intensities calculated in table 4.2 are not relevant. Therefore, the model takes into account the amount of rain fallen per hour multiplied by C_R=0.5 and A, half of the total area of the region (1.9 $[km^2]$) (see figure 4.3). And the discharges range between 5.27 and 13.2 $[m^3/s]$.

Stream initial and boundary condition temperatures

Upstream DTS temperatures are used for the upstream boundary condition. DTS temperature measurements along the stream are used as initial condition for the model.

[2]Dr. Dial Niang, Institut International d'Ingenierie de l'Eau et de l'Environnement, Ouagadougou (Burkina Faso)

Chapter 5

Data analysis

Stream temperature behavior has been studied since summer 2009. Before modeling temperature, we need to know how it is linked with special events. This is the aim of this section. The analysis of temperature evolution in time and space allows to see the overall dynamic of stream temperature.

5.1 DTS raw data analysis

On 21 June 2009, a long duration rain event took place. Figure 5.1 and 5.2 show the temperature data of this event. Figure 5.1 is a plot of temperature profiles along the stream recorded by the DTS optical fiber. There are many peaks that reveal, above all, the locations where the optical fiber is "in the air" and not inside water. The plot starts 200 [m] upstream from the DTS start and finishes at 1400 [m] upstream in the canyon (see figure 2.2). At the onset of rain (01 a.m.) and for the next two or three hours we see a nearly constant temperature all along the channel. This constant temperature is similar to the rainfall temperature.

If we remove peaks we have the gap plot in figure 5.2. Again the profile trend is flat in space and temperature decreases in time as we go forward in the night. Taking another rain event (figures 5.3 and 5.4, June the 29.) we see that warm water enters upstream (around 1400 [m]).

Using the same filter than before for figure 5.2 we clearly see on figure 5.4 that upstream water increases stream temperature during the rain event of June the 29. As we still move forward in the rainy season, more precipitation falls and soil water storage increases, new springs appear along the stream, as we can see in figures 5.5 (see arrows) and 5.6 but also slightly in figures 5.3 and 5.4.

Three springs seem to pour into the river on July 24. (see the three peaks on figure 5.5). The first peak is at 500 [m] from the start. The second one is at 960 [m] from start, and the last one (upstream) is at 1400 [m]. The main characteristics that allow the prediction of a confluence are (**1**) an almost constant stream temperature in time followed by (**2**) a smooth decrease in space as well as (**3**) a spring temperature almost equal to 29 °C and finally (**4**) a cooling trend on springs and a warming trend in other regions in the river (during rain events).

It has been shown [13] that in this area, ground water temperature decreases slightly along the rainy season from a little 30 °C to a 28 °C in average. These temperatures were measured in wells [11] at Tambarga (about in a 300 [m] radius away from stream, see figure **??**). However, as these temperatures are similar to the ones of springs, we assume that they are correlated. It means that groundwater temperature is constant with depth and that temperatures measured in wells effectively correspond to groundwater temperature.

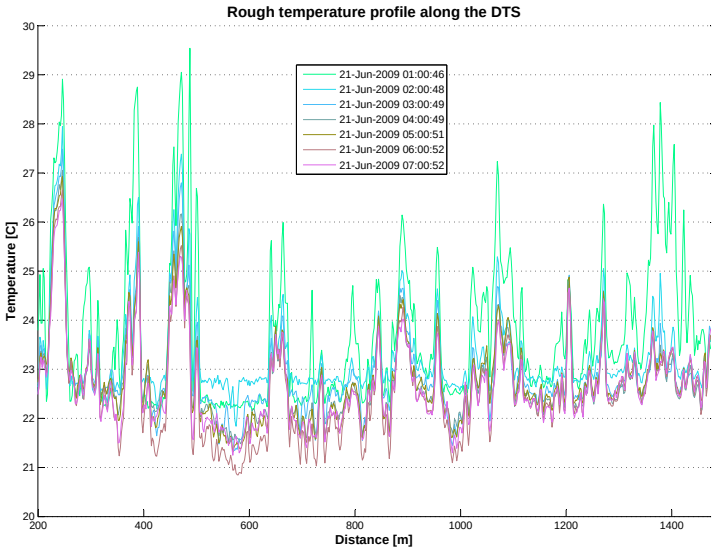

Figure 5.1: **Temperature profile along the river during a rain event measured with DTS (21 June). 1,400 [m] is the upstream end of the fiber cable**

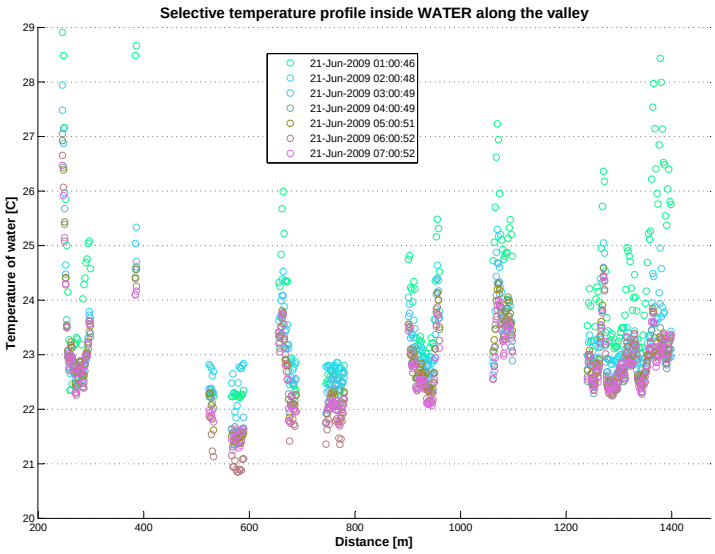

Figure 5.2: **As figure 5.1, submerged cable sections only**

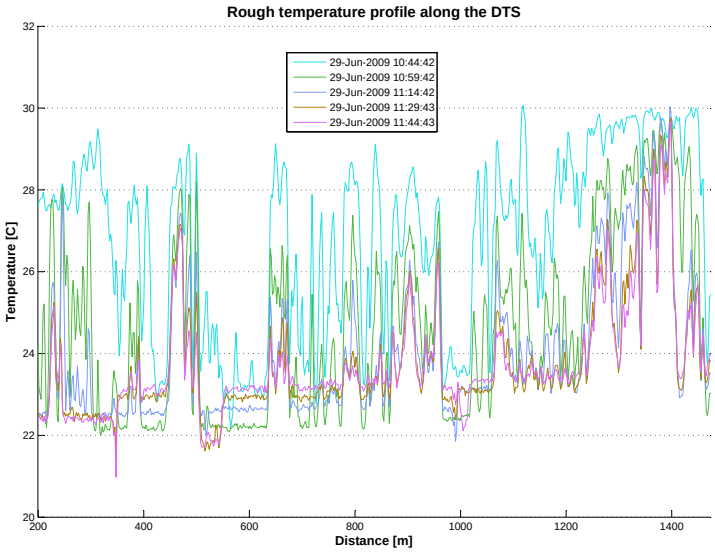

Figure 5.3: **Temperature profile along the river during a rain event (29 June) measured with DTS**

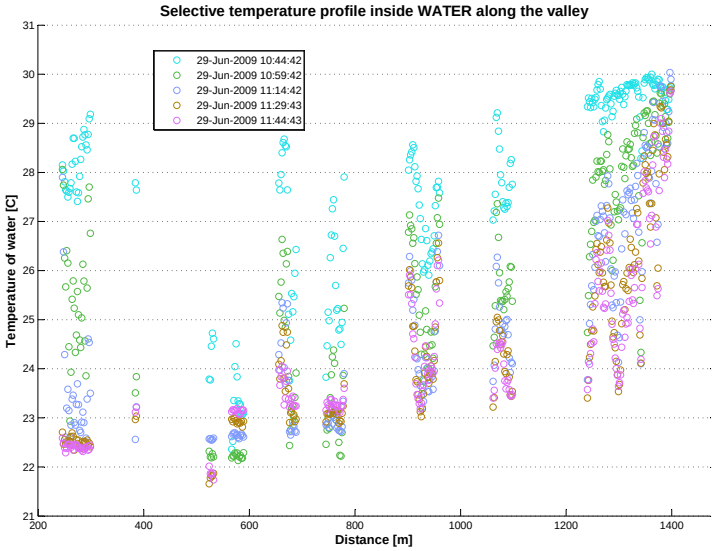

Figure 5.4: **As figure 5.3, submerged sections only**

.

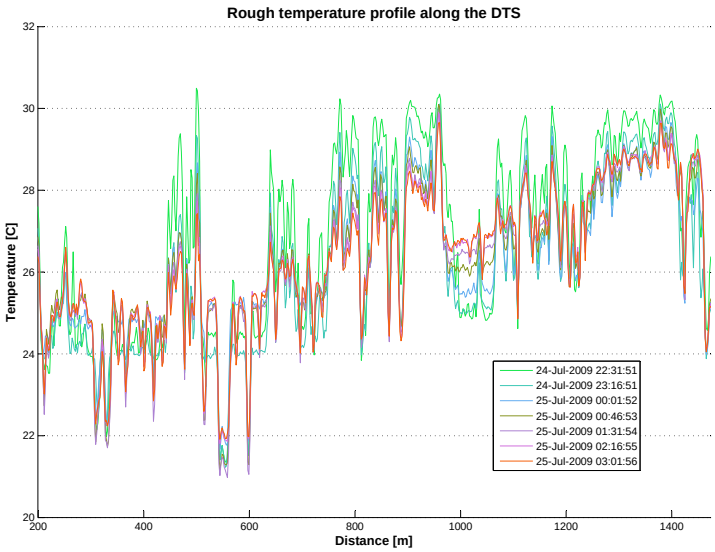

Figure 5.5: **Temperature profile along the river during a rain event (24 July) measured with DTS**

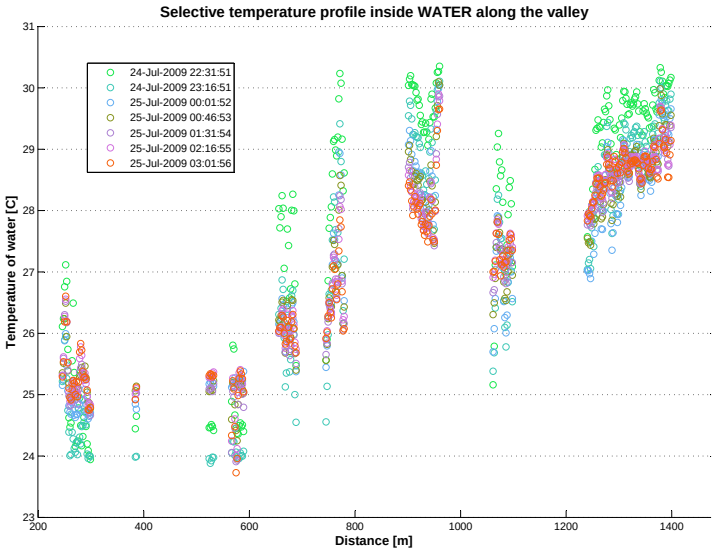

Figure 5.6: **As figure 5.5, submerged sections only**

5.2 Conclusion of the DTS data analysis

Although we assumed a single upstream spring, we saw that there are other water inflows. However, we **can not distinguish** from these graphs, the origin of the spring water. It can come from the groundwater (deep water) as well as from subsurface flow. Therefore, the stream water modeling will progress step by step. We will first start to model stream water temperature with a single spring upstream at a temperature given by the DTS optical fiber, as upstream temperature condition. For this we will consider periods without rainfall that presumably will not give spring into the main river. For this reason, these first simulations will be done early in the rainy season.

Once the model is calibrated and gives a similar temperature profile, in space and in time, like the one measured by the DTS optical fiber, we will add springs assuming that they represent subsurface flow ($\neq$ groundwater flow). Subsurface flows have, by assumption, a temperature equal to the one measured in the fields by station 1009, near MET 1 (on the hill, see figure 2.2) at a depth of 10 [cm]. We are forced to make this hypothesis as Tidbits miniloggers (see figure 2.6) did not work long enough to cover all the rainfall season. Another hypothesis will also be done on the springs' discharge as they were not measured during that summer. We will make new simulation for early July, when we are sure that water was flowing inside the river but presumably before ground water resurgences started contributing to stream flow. The previous hypothesis will be discussed.

Finally, if the previous stage has given satisfactory results according to the assumptions we made, the next modeling step is to include groundwater flow into the main stream. We shall implement it in such a way that the results will approach the "reality", that is to say the DTS optical fiber measurements.

5.3 Single sensorscope hypothesis

Concerning the hypothesis of using only station 1000 for input data, we check its relevance here. Solar radiation measured at sensorscope stations 1000 (see figure 2.2), 1007 (downstream), 1009 (on the hill) and 1015 (entry of the canyon) (see figure 2.2) is shown in figure 5.7. If the measured data are similar at different sites for the solar radiation, air temperature, air humidity and wind speed parameters, we can assume that MET 2 (see figure 2.2) measurements are representative of all the basin. Solar radiation (see figure 5.7) records are similar for a five days period. The hypothesis is good for this case.

The air temperature is similar at all for stations with a maximum difference of 1 °C with a smaller variation in the plain than in the canyon (station 1009 in red on figure 5.8). Even in case of a rainfall, air temperature is nearly equal, no matter the measuring point. Again, the assumption, that station 1000 is representative of the catchment, is verified in this case.

Air humidity (see figure 5.9) has bigger variations among the different locations where it was measured. Especially on June 20^{th}, while the rainfall event, the sensor on station 1000 did not work well and we have the air humidity dropping to 10%. Apart from this single occurrence, we see that the air humidity is a little lower at station 1000 as its temperature was lower also (see figure 5.8). A lower air temperature limits the air vapor pressure at a lower value (see equation 4.2). As the assumption used the value of station 1000 only, it underestimates the actual air humidity. This affects the evaporation rate positively. A bigger evaporation brings a bigger cooling to the water and for this reason, stream temperature model might cool too much the river.

Finally, the wind speed (figure 5.10), has important variations according to the locations where it was measured. The plain (station 1000 and 1007) has the highest wind speed whereas station 1009 (on the hill) has the lowest wind speed. This statement can be surprising, however, the hill has much more vegetation (small trees and bushes) than the plain. This may limit the wind speed at this location.

Station 1015 (at the entry of the canyon) has a wind speed in the middle of the two described before. If we consider only the tree stations (**1000, 1007** (and 1015)) at the altitude where stream water is flowing (mainly station 1000 and 1007) we see that the wind speeds have little variations (less than 0.5 [m/s]). However, in the canyon, the wind speed is overestimated. This increases also the latent energy flux and the river might cool down

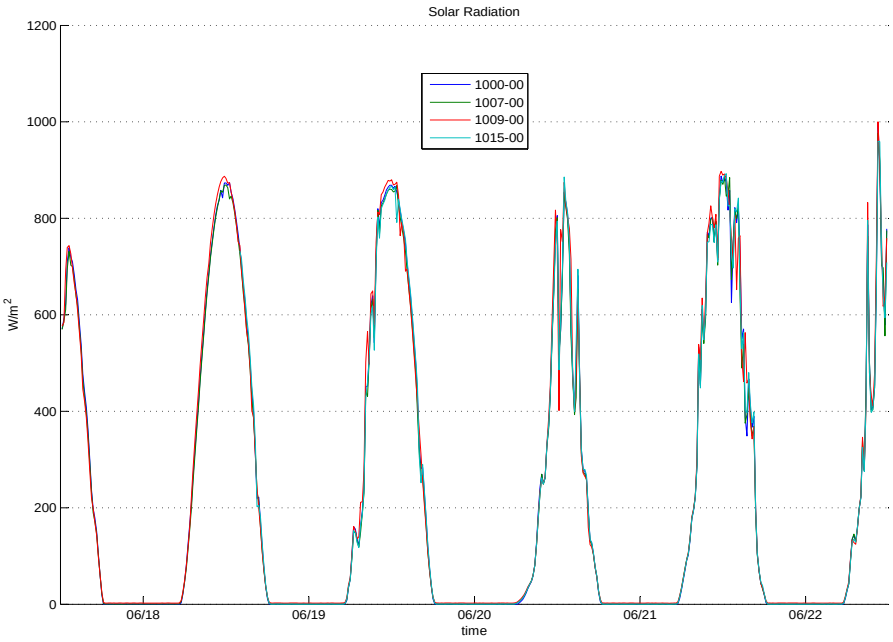

Figure 5.7: **Comparison of solar radiation measured at different locations in Tambarga's basin**

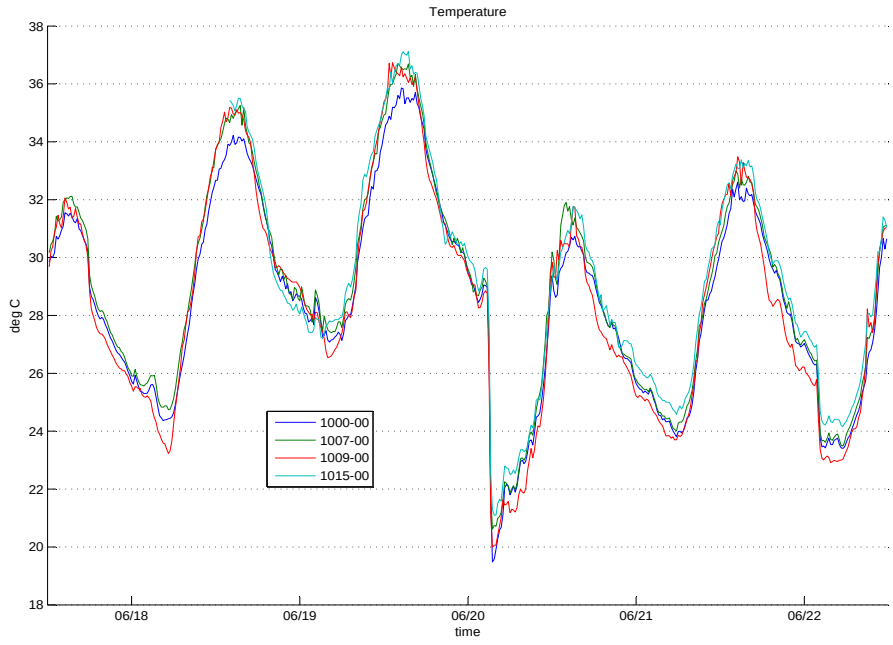

Figure 5.8: **Comparison of air temperatures measured at different locations in Tambarga's basin**

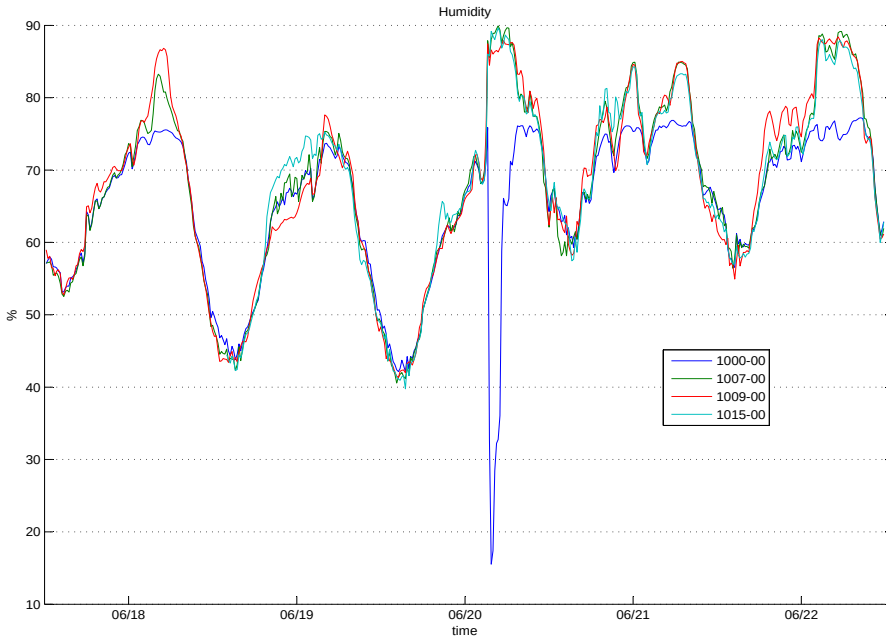

Figure 5.9: **Comparison of air humidity measured at different measurement points in Tambarga's basin**

too much.

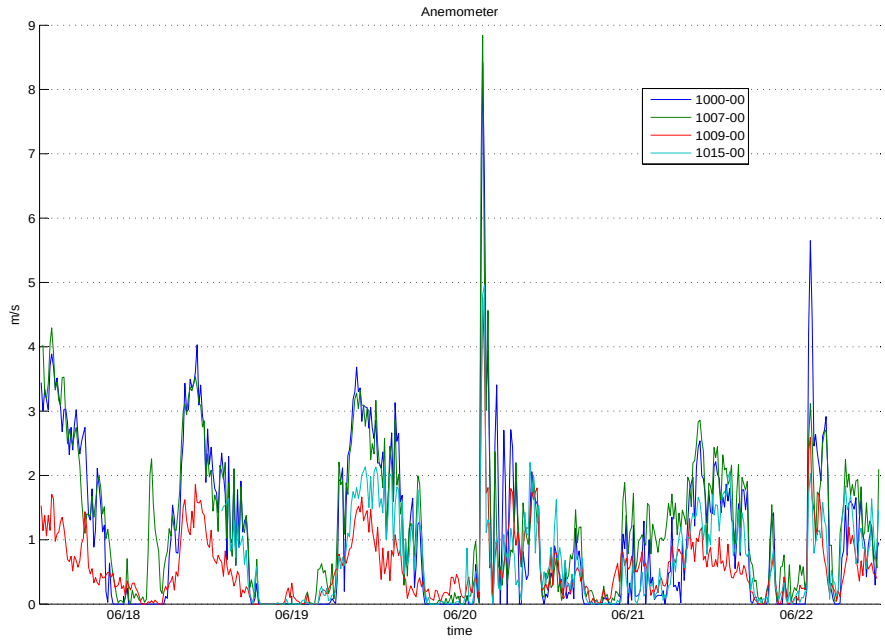

Figure 5.10: **Comparison of wind speed measured at different locations in Tambarga's basin**

Chapter 6

Stream temperature simulation results

The mass and energy balance aims to determine the discharge of the river but also the one of the springs entering. Step by step, starting with a single spring bringing water into the main river, we will compute here the temperature profile along the stream and compare it to DTS data collected in the same river at the same time. To get a profile of temperature along the stream, we partitioned it in many small volumes on which we shall apply the complete energy balance at a given time step. As a first attempt, we introduce one inflow upstream. When the model give satisfactory results compared to measured temperature, we shall keep on adding new tributaries to the main river.

6.1 Simulation without rain, subsurface flow and ground water

Description

At the beginning of the rainy season, the water table is low enough to prevent any upward heat transfer (by convection) into the river. As river flows, some of its water percolates into the stream bed (also cold sediment) and enters again into the stream some meters downstream. A temperature gradient between stream temperature and sediment temperature determines the heat conduction ($\phi_{conduction}$, see equation 6.1) into the stream bed. At this stage, the alluvium has a lower boundary layer leading to the deeper alluvium which is set with a constant temperature. It represents a big reservoir with a sink (daytime) or source (nighttime) of energy to the river.

$$\phi_{conduction} = -\frac{K_{soil}(T - T_{soil})}{d_{soil}} \tag{6.1}$$

K_{soil} is the thermal conductivity of the **saturated** sediment of the stream bed, T is the river temperature, T_{soil} is the temperature of the sediment and d_{soil} is the **sediment's depth** (see figure 6.1) below the water.

The sediment depth is a parameter with large impact on model results. Indeed, as we will see in the simulation results, the temperature gradient between water and sediment can be of 10 °C when discharges are small compared to the energy balance acting on it. Using equation 6.1, if we consider a sediment's depth (d_{soil}) of ten centimeters (0.1 [m]) and a temperature gradient of 10 °C we have already a heat conduction of order 2 (O^2) as this ratio gives 100. Largest conductive fluxes occur in the most downstream part of the river where temperature gradient between water and soil can be significant. A sediment's depth of 0.3 [m] gives a heat conduction $\phi_{conduction}$ of 20 [W/m^2], whereas for d_{soil}=0.1 [m], $\phi_{conduction}$ reaches almost 200 [W/m^2]. Finally, d_{soil} has been calibrated and set as a constant in order to get a best fit temperature profile along the stream. After many simulations of a two days period, we set d_{soil}**=0.3 [m]**. d_{soil} is used to enhance the accuracy of the model and its value, in this study, does not rely on any measurement.

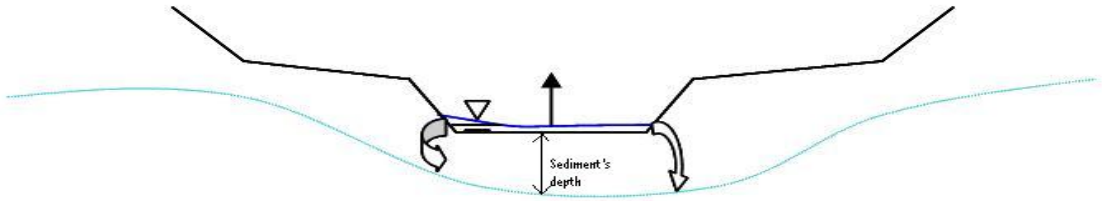

Figure 6.1: **Crossection of a stream: Stream water percolates when groundwater table is lower than stream bed level**

Results

First, all the components that led to stream water temperature will be explained. Later, only stream temperatures will be discussed.

The stream is divided in four different segments according to dominant energy balance components (see figure **??**). The available net energy (ϕ_{total} in equation 3.3) appears in red in figure 6.2. Dotted pink lines are the solar radiation (short wave) measurements and the continuous blue lines are the short wave radiation reaching the stream water. Their values at night are zero. The net radiative energy on the river varies because of shadow coefficients, land cover fractions and losses into the stream bed. These values are calculated using parameters of table 4.1 and equations presented in **section 4.2**. Black lines represent the latent heat flux. The negative sign of evaporation means that stream water is losing energy. Latent heat reaches a maximum value, when solar radiation is maximum. Sensible heat flux, in green, is around zero. The heat conduction into the stream bed (in light blue) increases from upstream to downstream reaches on the river. As the temperature variation is very important (sometimes 10 °C), the heat conduction amounts to 20 $[W/m^2]$. Again a negative sign means that water loses energy to the river bed. The remaining term (in red) behaves as expected for the three upper reaches. Water cools down at night and warms up with the sun during the day. However, in the most downstream part, the remaining term has a behavior similar to a soil. Heat conduction into the ground prevents the stream from warming during the day. Early in the morning, however, the temperature gradient between water/bed interface is smaller and the energetic balance (in red) is nearly zero.

All components of the energy balance are displayed in figure 6.2. The residual energy (c.f. equation 2.2), in red color, changes according to the characteristics of river's neighborhood. Logically, during the day, the available energy is positive. This means that stream water is gaining some energy, whereas at night, this available energy term is negative. Stream water is cooling down because of the energy deficit. The fact that we make the energy budget on a wet surface leads to a quasi nil sensible heat flux. Indeed as soon as the water starts storing energy, this latter is used for evaporation. The latent heat flux is therefore very large compared to the sensible heat flux. As none of the energy component shown on this plot, is negative at night, the cooling effect is the result of a negative balance of the long wave radiations.

The details of long wave radiation are shown in figure 6.3. In green, the net long wave radiation varies between zero and -100 $[W/m^2]$. Long wave emitted by the water (in blue) or by the land coverage (in red) are nearly similar for every compartments along the river. Yet, long wave radiation from the atmosphere (in black) varies a lot. Long wave radiation released by the water present some very smooth curves. This is because they are calculated from stream temperature and the model has a smoothing effect on stream temperature profile. Other curves are calculated from the measured meteorologic data.

For this simulation we did not take into account any subsurface mass flow nor ground water flow, we just compare (in figure 6.4) modeled downstream temperatures with the measured one. At this place, real discharge can be compared to the assumed discharge of 20 [l/s].

For a downstream location (see figure 2.2 red line), we obtain quiet similar curves for modeled and measured

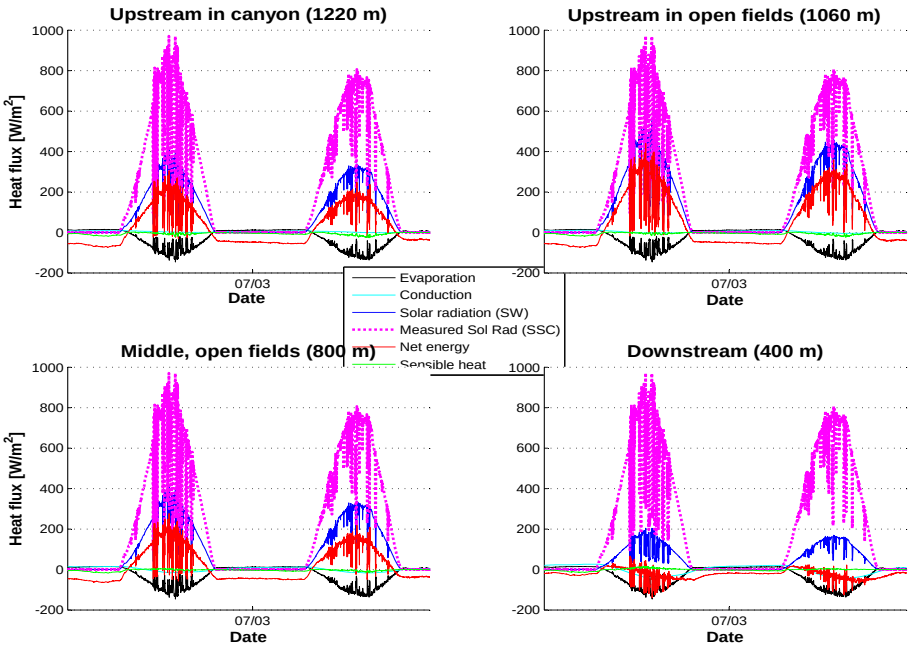

Figure 6.2: **Energy balance components computed from meteorologic measurements at 4 locations along the stream**

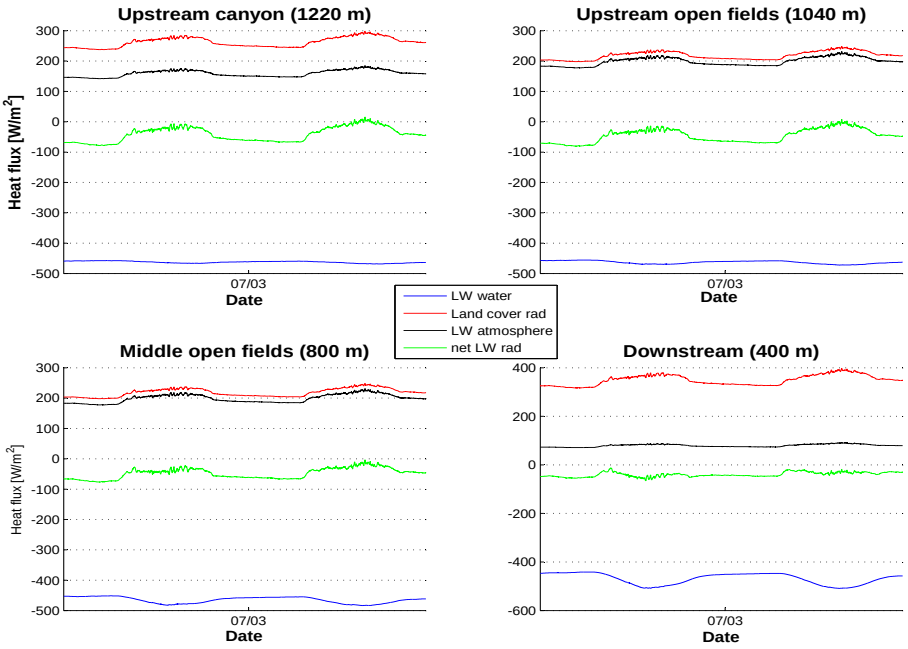

Figure 6.3: **Long wave radiation computed from meteorologic measurements at 4 locations along the stream.**

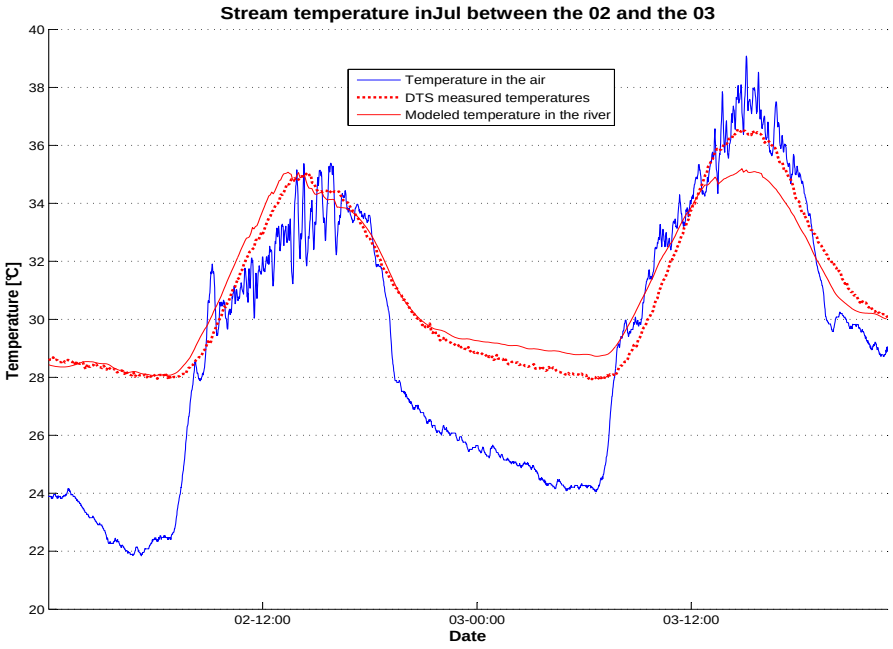

Figure 6.4: **Modeled and measured stream temperatures compared to air temperature during two days at the downstream location (see figure 2.2).**

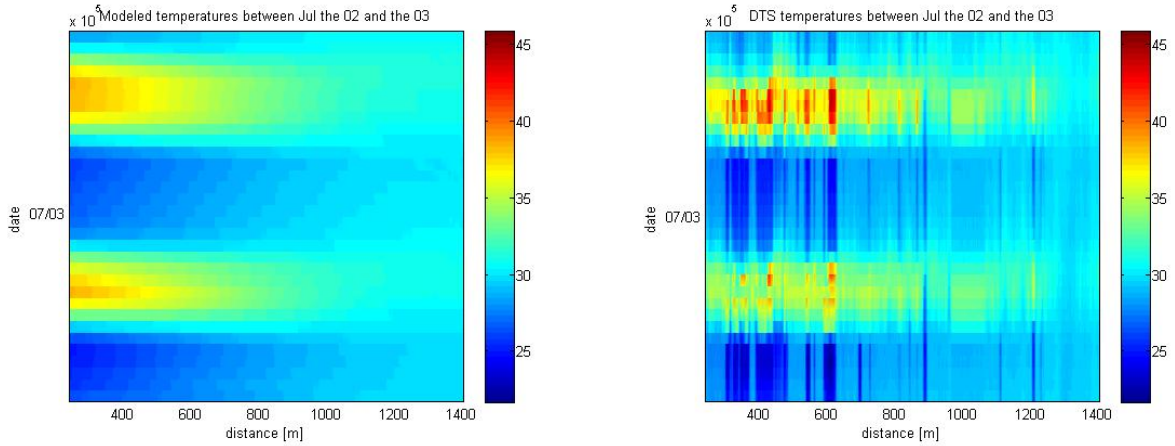

Figure 6.5: **Temperature evolution in time and space from July 2^{nd} to July 4^{th}. Left panel: modeled temperature. Right panel: DTS measurements. Recall that 1,400 [m] corresponds to the upstream location.**

temperatures (see figure 6.4). On July 1, a rain of 24 [mm] fell on the basin. As the model does not take into account subsurface flow but only the constant upstream discharge at upstream temperature, there is a slight difference during the first night. Indeed, as water spend some time inside the soil, it warms up a little and, consequently, warms up the river. As time goes by, water stored in the soil diminishes leading to a decreasing contribution to the stream. The discharge decreases and temperature variation increases. Therefore, on the second day, modeled temperature under-estimate measured stream temperatures. The fact that solar incoming radiation for the second day is smaller than for the first day (see figure 6.2) confirms this hypothesis.

Figure 6.1 shows the evolution of modeled and measured temperature along the observed reach. Next simulations will be computed with longer time span. This illustrates better the characteristics of the stream temperature behavior in time. Doing so, we understand better the effects of the rain (direct and indirect runoff) on stream temperature.

6.2 Simulation without ground water

Description

At this stage, stream temperature modeling will take into account rainfall flow (runoff) and subsurface flow. Although the groundwater table might have risen up, the sediment's depth remains at 0.3 [m]. It is assumed that runoff and subsurface flow use the same channels to reach the main stream. The locations of confluences are determined from the previous study (see figure 5.5) at distances 960 [m] and 500 [m], from DTS instrument.

the influence area of the most upstream spring is nearly 272'500 $[m^2]$ (27.25 [hectares], in evidence in red on figure 6.6, calculated from the GIS map). For this area ("Source 2" in figure 3.5), we set a constant spring discharge of 0.02 $[m^3/\text{s}]$ (see figure 6.6).

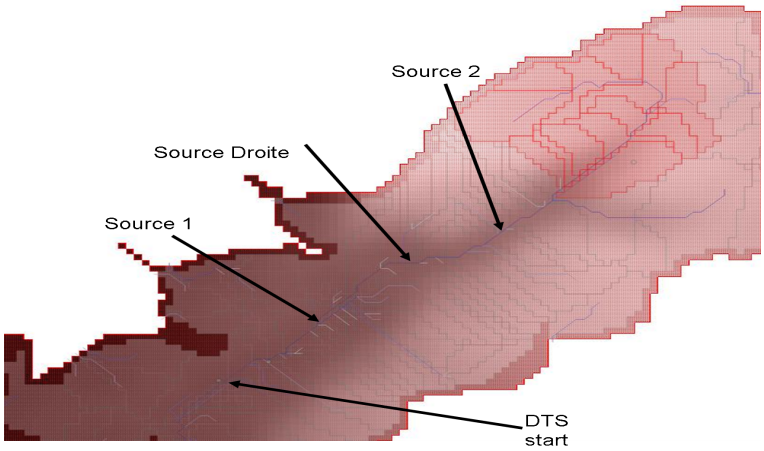

Figure 6.6: **Drainage area of "source 2"**

To be consistent in spring discharge characterization, we set here a discharge to area factor that is defined as follow;

$$f_{QA} = \frac{Q_{spring} \quad [\frac{m^3}{s}]}{A_{tot} \quad [km^2]} = \frac{0.02}{0.27 + 0.213 + 0.13} = 0.033 \quad \left[\frac{m^3}{skm^2}\right] \tag{6.2}$$

For "Source 2" (see figure 3.5 and 6.6), the area of contribution is 0.27 $[km^2]$ and the discharge is calculated as follows:

$$Q_{Source2} = A_{Source2} f_{QA} = 0.27 * 0.034 = 0.0091 \quad [m^3/s] \tag{6.3}$$

For "Source droite" , the contribution area is about 0.213 $[km^2]$. Considering the same "discharge to area" factor, we obtain a corresponding discharge, Q_{SD}=f_{QA}0.213=0.034*0.213=**0.0072** $[m^3/s]$.

A third spring ("Source 1") appears downstream (see figure 6.8), with a drainage area of 0.13 $[km^2]$ and the discharge is estimated at **0.0042** $[m^3/s]$.

These calculated discharges will be used in the temperature model that consider subsurface flow and flow due to rainfall. Rainfall is injected as an additional discharge for the time of the rainfall event. Additional discharge during the rain event is dependent on the precipitation rate throughout the event.

All the references on the last figures are shown in figure 3.5.

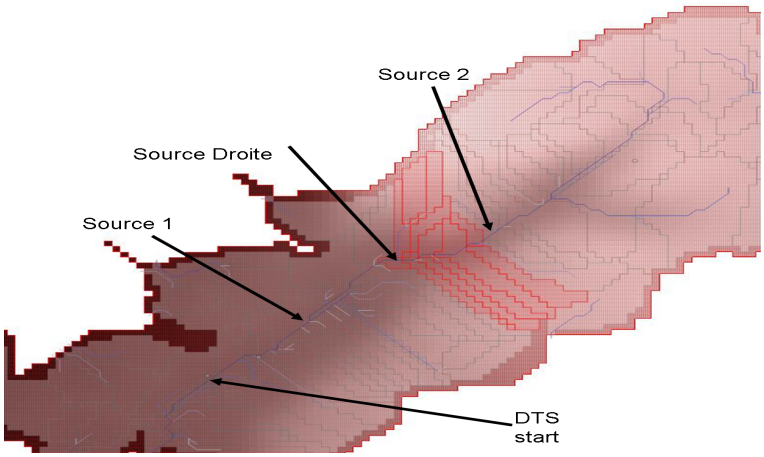

Figure 6.7: **Drainage area of "source droite"**

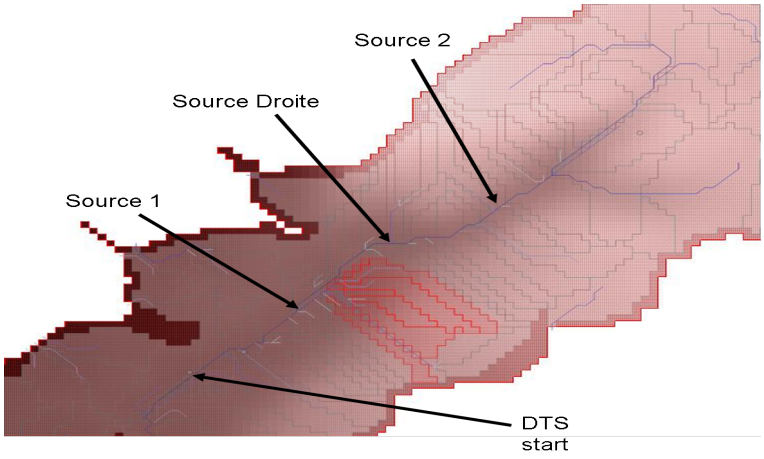

Figure 6.8: **Drainage area of "source 1"**

In order to have "good" results the shadow coefficient, C_s, is changed to value shown in table 6.1. Increasing the shade (upstream) diminishes the solar radiation effect on stream temperature.

Parameters	$Upstream$	$Middle(up)$	$Middle(down)$	$Downstream$
C_s	0.50	0.45	0.4	0.30
θ_{VTS}	0.4	0.5	0.5	0.2
D_f	0.40	0.40	0.30	0.30

Table 6.1: Coefficients for shadow (C_s), sky view (θ_{VTS}) and bed conduction (D_f) into the deeper alluvium coefficients

Results

A five days simulation for stream temperatures, at the beginning of July 2009, gives the results shown in figure 6.9. The dotted lines ("Upstream", "Middle" and "Downstream") represent the data collected by the DTS, whereas the continuous lines are the results of the simulation. As we put the upstream DTS data as boundary condition, the model upstream section compares well with measurements (blue lines on figure 6.9).

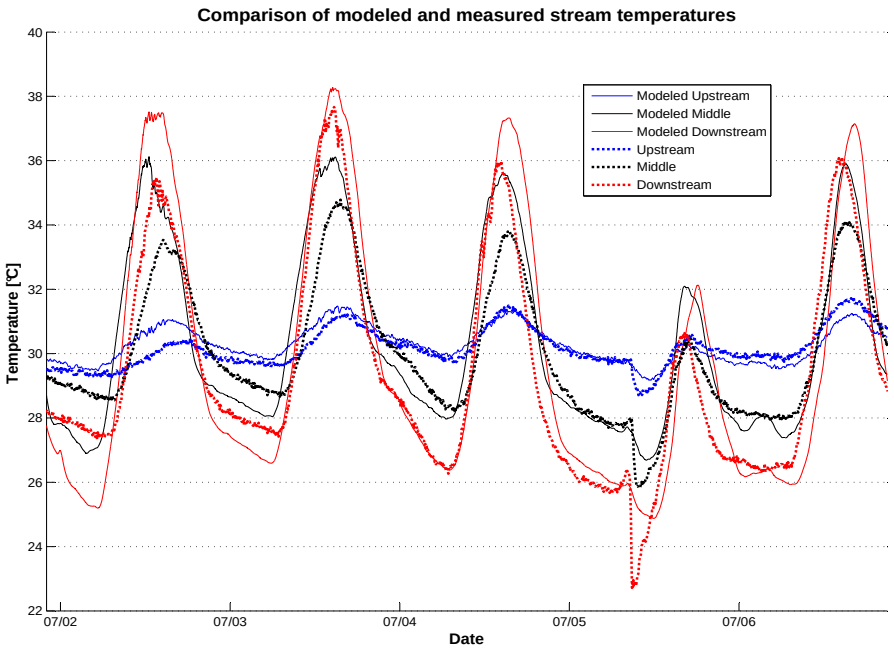

Figure 6.9: Modeled temperature compared to DTS measured temperatures for the 3 locations along the stream (see figure 2.2).

As we move downstream to the "Middle" section, we see already a slight (0.5 °C), **but constant**, temperature difference between modeled and measured temperatures. Furthermore, the amplitude of temperature is smaller for the measured data than for the modeled one. This can be corrected by adjusting the discharge. At this place, the discharge, Q, is 0.0091 $[m^3/s]$ (1 spring out of 3 has come into the river) and it may underestimate the actual discharge. For this reason, the temperature fluctuates with a bigger amplitude in the model than in reality.

Then, the red lines are taken in the downstream section where all three springs have come into the river and the discharge there is 0.0205 $[m^3/s]$. At this place, we see that the temperature difference is not constant in time. Large at the beginning, the temperature difference (at night) decreases in time. During the day, temperature differences are varying between 1 and 2 °C.

Finally, on July 5 2009, the morning rain is not correctly modeled for the "middle" and "downstream" section. This might be due to the fact that the runoff discharge is not taken into account in this model.

Going further in the analysis of the "downstream" temperature, we see in figure 6.10 that DTS measured temperatures are much more dependent on air temperature (in blue) than the modeled one. The simulation seems not accurate for the effect of air temperature on stream temperature. Inaccurate representation of the modeled sensible heat flux may be a cause for the discrepancy.

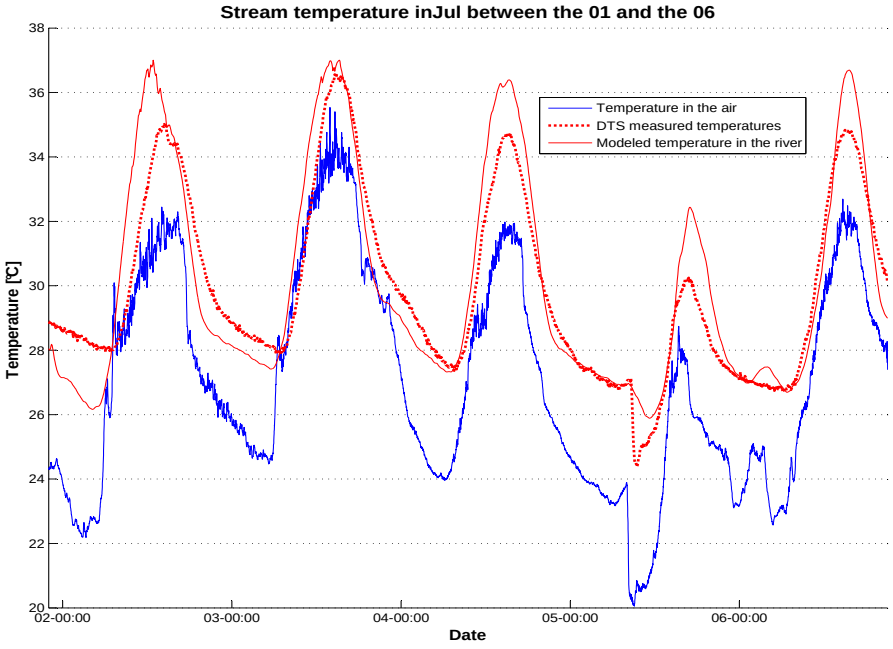

Figure 6.10: Modeled and measured temperature at the downstream location (in red) compared to air temperature at station 1000 (see figure 2.2)

The net insolation of the stream (in blue) does not vary too much during the three first days of modeling (see figure 6.11). As stream temperature follows the same trend, we can notice that the model is much more linked to solar radiation than to air temperature. Furthermore, the sensible heat flux (in green) is close to zero, all the time.

As we added constant discharge springs in this simulation, we study here their effects on the stream temperature profile. We clearly see on the left panel of figure 6.2 where the tributaries enter. Although three springs are flowing into the river, the DTS plot (right panel) shows only two clearly. Three springs are modeled because of the results from DTS raw data analysis (see figure 5.5). The spring temperatures correspond to the temperature measured by station 1009 (close to MET 1 on the hill) at a depth of 0.1 [m]. Indeed, we assumed that the water

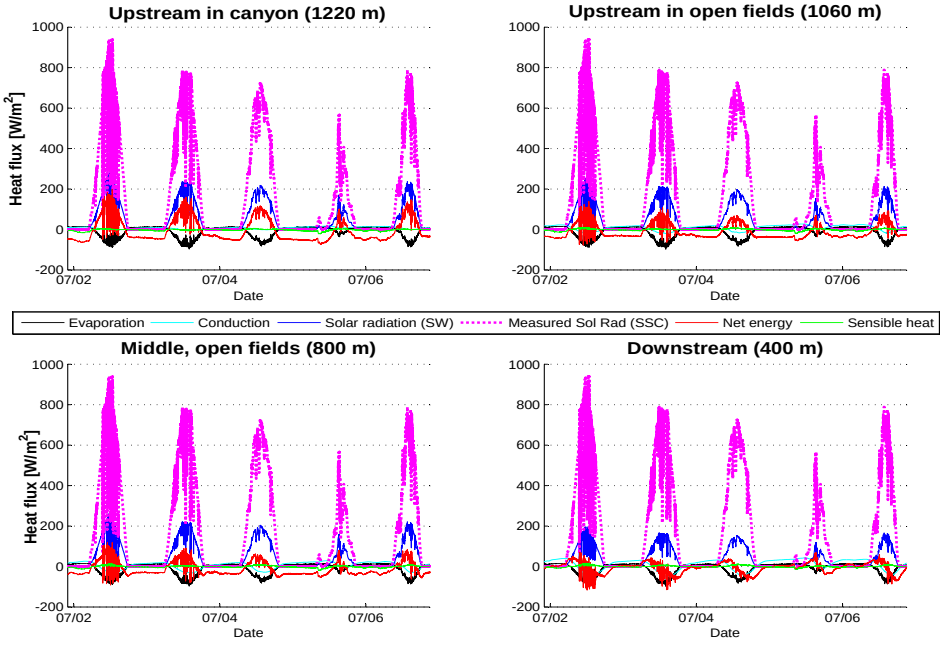

Figure 6.11: Energy balance components computed from meteorologic measurements at 4 locations along the stream.

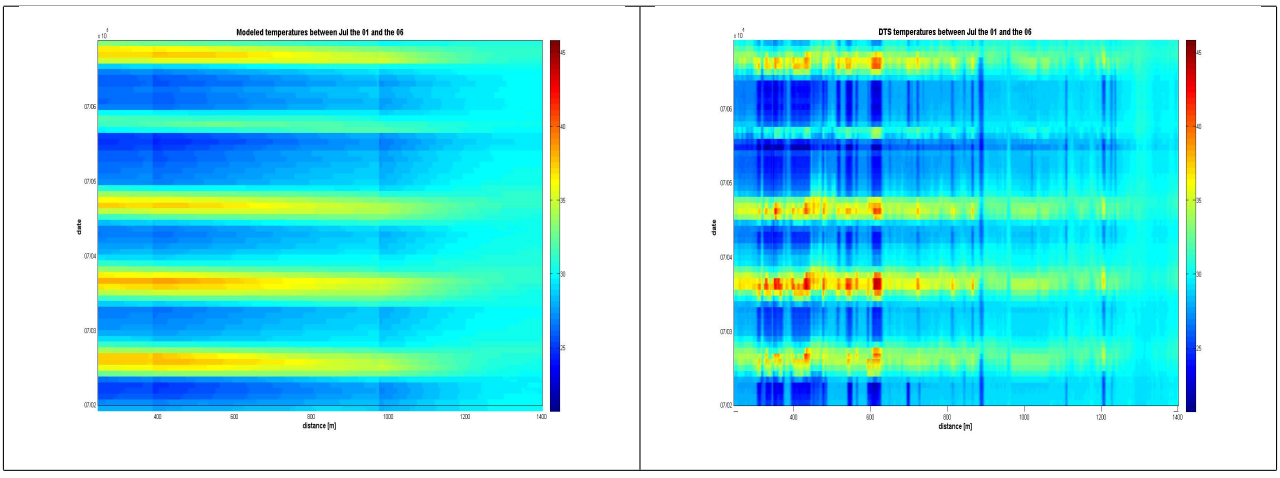

Figure 6.12: **Temperature evolution in time and space from July the 6. to the 16. Left panel:Modeled temperatures. Right panel: DTS measurements**

coming out at the two upstream springs entered in a soil similar to the one on the hill. For the spring downstream, the temperature is the one taken at 0.1 [m] depth, but at station 1000 (see figure 2.2).

Another way to illustrate the effect of springs on stream temperature is shown in figure 6.13 for three different nights. If we plot the modeled and measured stream temperatures over the total length of the river, we can see the profile of temperatures at the spring points. DTS measured temperatures present a lot of "noise" which does not help for comparison. However, points of confluence appear very clearly as all temperature profiles have the same local trend.

Soil temperature at 0.1 [m] depth (upstream on the hill) having an average between 29 and 30 °C confirms the plotted profile (in figure 6.13), with a confluence temperature around 30 °C for the two upstream springs.

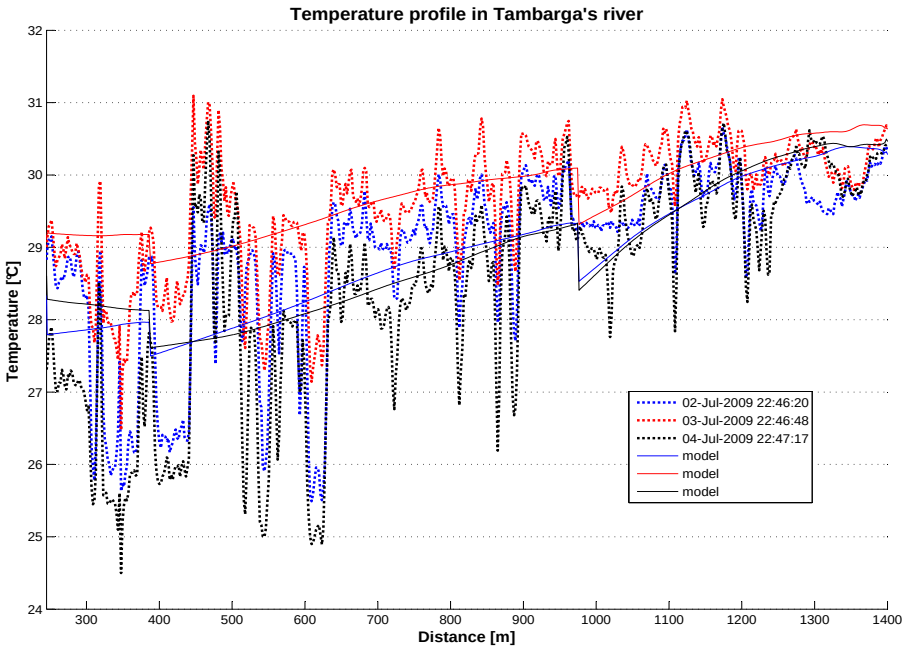

Figure 6.13: Comparison of modeled and measured temperatures at different times along the river.

Equation 6.4 in [19](Selker J.S. et al, 2006) gives a relation between the ratio of upstream discharge to spring (or groundwater) discharge with downstream temperature, T_o^j.

$$\frac{Q_i^j}{Q_g^j} = \frac{T_o^j - T_g^j}{T_i^j - T_o^j} \tag{6.4}$$

Water entering the control section has subscript i, outflow has subscript o, and groundwater inflow has subscript g. If we take the "red" line in figure 6.13, we have for the second spring (at 960 [m]);

$$T_g^j = T_o^j - (T_i^j - T_o^j)\frac{Q_i^j}{Q_g^j} = 30 - (29,4 - 30)\frac{0,0091}{0,0072}, \tag{6.5}$$

since we look for the spring inflow temperature, T_g^j, this gives a **temperature of 30.5** °C and this is the temperature of the spring. Interestingly, this is nearly the soil temperature upstream in the canyon.

Summary

We could see that adding local springs with a constant discharge in time and a temperature corresponding (by assumption) to the soil temperature at 0.1 [m] depth, improves the simulation results. This is especially true for the upstream section containing the two first springs. Yet, as we reach the third spring (downstream) we see that we have an effect of varying temperature difference over time between the model and the measurements. **This means either that the third spring has a discharge varying in time dependent on the soil water content**, or the temperature of the deeper soil decreases day after day and releases cooler water into the stream.

If we make the same simulation over a ten days period (see figure 6.14) we clearly see exactly this trend. Plus, we can notice that the spring discharge variance is due to rain events. The space between the two green lines decreases with time (since the last rain event). Just after a rain event, the soil heat capacity is enhanced because of a higher soil water content. The cooling of the soil is smaller and the rate of cooling (slope of the green line in figure 6.14) is small. When the soil water content decreases, the soil cools down quicker and the rate of cooling increases.

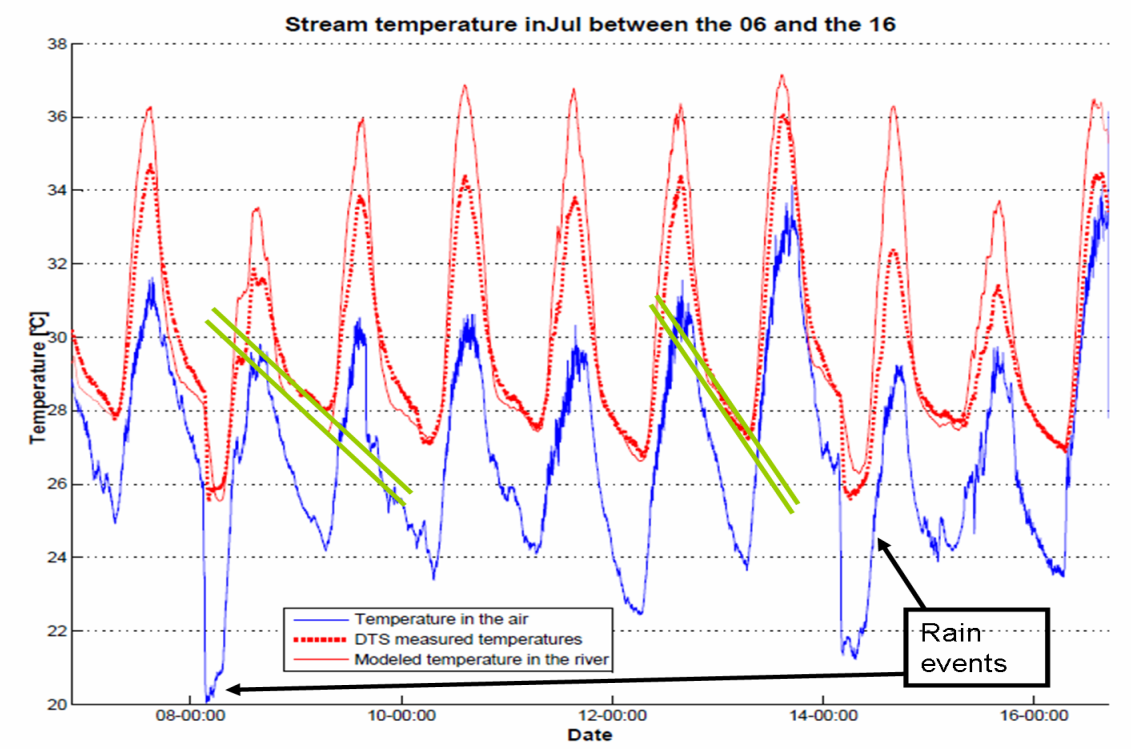

Figure 6.14: Modeled temperature and measured air temperature at a downstream location at station 1000 (see figure 2.2)

In this simulation, we did not take into account groundwater incomes into the river. It turned out that it is difficult to consider ground water inflow as we do not have any indications of the locations of resurgence nor measurements of the groundwater temperature. Figure 6.15 shows temperatures measured in different wells as well as the depth of the water inside the wells during summer 2009. Most temperatures vary between 29 and 32 °C in June, but decrease slightly with the rainy season. However, this range of temperatures confirms the temperature of 30.5 °C calculated with equation 6.5 for the subsurface inflow temperature.

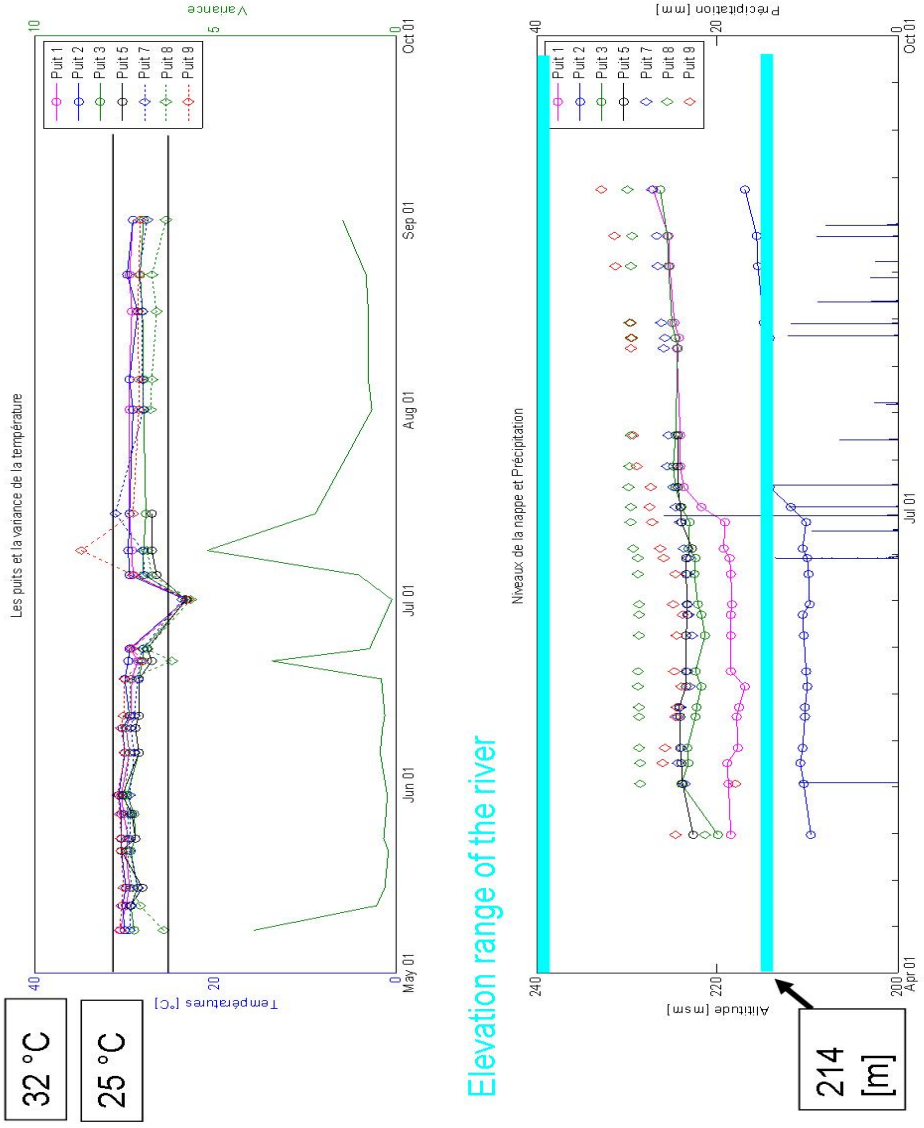

Figure 6.15: **Water level and temperature in different wells in the Tambarga area during summer 2009.**

6.3 Simulation of stream temperature considering all processes

Description

For this last modeling stage we take into account the subsurface flow and rainfall generated surface runoff. To this end, we set d_{soil}=0 (or sediment's depth in figure 6.1) in the "plain" (crop area) of Tambarga's river, as groundwater table is higher than the stream. Figure 6.16 illustrates this situation.

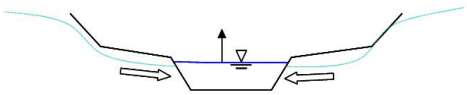

Figure 6.16: **Crossection of a stream: groundwater enters into the stream when groundwater table is higher than stream bed level**

The runoff (after a rain event) decreases with time. Temperature of runoff water is again, identical to the one at 0.1 [m] depth in the soil at MET 1 or MET 2. Starting runoff discharges were given in table 4.3. Runoff temperatures are constant in time by assumption. Only the discharge decreases exponentially with time to reach the previous values used in the last simulations.

Chapter 7

Accuracy assessment

Table 6.1, presents the coefficients used for the last simulation. Namely, the shadow was enhanced in the "upstream" and "Middle(up)" region which is more similar to reality as we have trees and bushes all around the river in these regions. When the upstream discharge was decreased, the model was able to warm up the water enough to simulate the real behavior. The modeled stream temperatures follow the general dynamic of the measured one. One apparent error of the model is that it cools down the river too much at night (see upstream part on figure 6.13). This can have many reasons as discussed below.

7.1 Cooling effect

As we can see on figure 6.11, the net energy balance (in red) is more negative in the most upstream part than in the others. The river bed conduction (in light blue) is nearly zero all day long. As we put a riverbed temperature equal to the spring temperature, hardly any heat flux can occur between the stream water and the river bed. The latent heat flux is an important factor for cooling the river, but at night this flux is zero. Consquently stream water cooling is mainly the result of the long wave radiation balance (see figure 7.1).

We see here that the net long wave radiation (in green) presents a negative budget, all the time. The "view to sky" coefficient (θ_{VTS}) is responsible for this effect. During the day, it prevents long wave radiation from the atmosphere from reaching the river surface, and at night, it controls the long wave emissions of the water (blue curves in figure 7.1). The fact that we reduced the incoming long wave radiation with the θ_{VTS} (this was not done in the original model [24]), made the overall long wave radiation balance negative. A measurement of the incoming long wave radiation over the river in this region (upstream in the canyon) could increase considerably the model accuracy. The value of θ_{VTS} in the canyon (one of the largest, 0.4) may overestimate the long wave radiation loss. Indeed, vegetation and rocks in the canyon may store much more energy, and release it during the night in a bigger amount than the model computes.

For the other sections further downstream, the cooling trends (see figure 6.13) are similar to the measured ones.

7.2 Springs location and discharge determination

The small discharge upstream allows stream temperatures to cool down very easily, but on the other hand it also allows to warm it up quickly in the morning. Considering different constant discharges for each segment along the river helped calibrating the model. Indeed, it gained in accuracy (see figure 6.9). However, we know that all the modeling basin is subject to subsurface flow variations. A rainfall impacts on stream temperature as figure 6.14 confirms. If the model would account for these varying additional flows, the results would be even

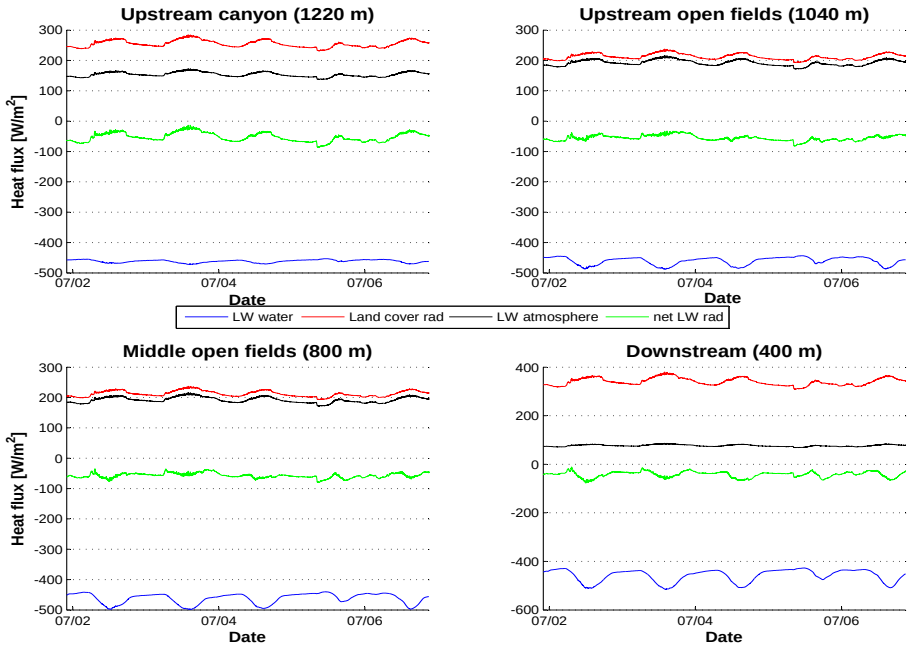

Figure 7.1: Long wave radiation computed from meteorologic measurements at 4 locations along the stream.

more accurate. As an estimation, the additional discharge (Q_{add}) reaching the river due to subsurface flow should depend on parameters presented in equation 7.1.

$$Q_{add}(t) = f(\theta, V_{soil}, K_{soil}) \tag{7.1}$$

θ is the water content of the soil, V_{soil} is the volume of soil that is drained and K_{soil} is the hydraulic conductivity of the soil. This latter depends on the current water content. The specific discharge per square meter in a non saturated soil can be expressed as ([15] Musy,1991);

$$\overrightarrow{q}_{non-saturated} = -K(\theta)\overrightarrow{grad}[h(\theta) + z] \tag{7.2}$$

Equation 7.2 has the parameters $K(\theta)$ and $h(\theta)$ which are difficult to estimate. The hydraulic conductivity ($K(\theta)$), function of the soil water content, presents a hysteresis behavior [15] between increasing and decreasing soil water content. The hydraulic head ($h(\theta)$) must have "monotone" behavior in the mathematical sense (i.e. continuously increase or decrease).

At this stage, it would be necessary to recognize whether the inflow water comes from the deep alluvium or if it rather comes from the subsurface. Figure 7.2 illustrates that time temperature evolution (here during ten days) corresponds nearly to a soil temperature dynamic. The amplitude decreases at the spring and the maximum temperature is delayed when approaching the spring. As we get further away from the spring, the temperature amplitude increases [12]. The spring inflow temperature (in green) varies little day to day. Its average temperature is around 30 °C. This is very similar to the results previously obtained in equation 6.5.

If we look at the second modeled inflow ("source 1" see figure 7.3), we see that none of the described situation is really occurring here. We have a slight decrease in the temperature amplitude (see the red line), but it still

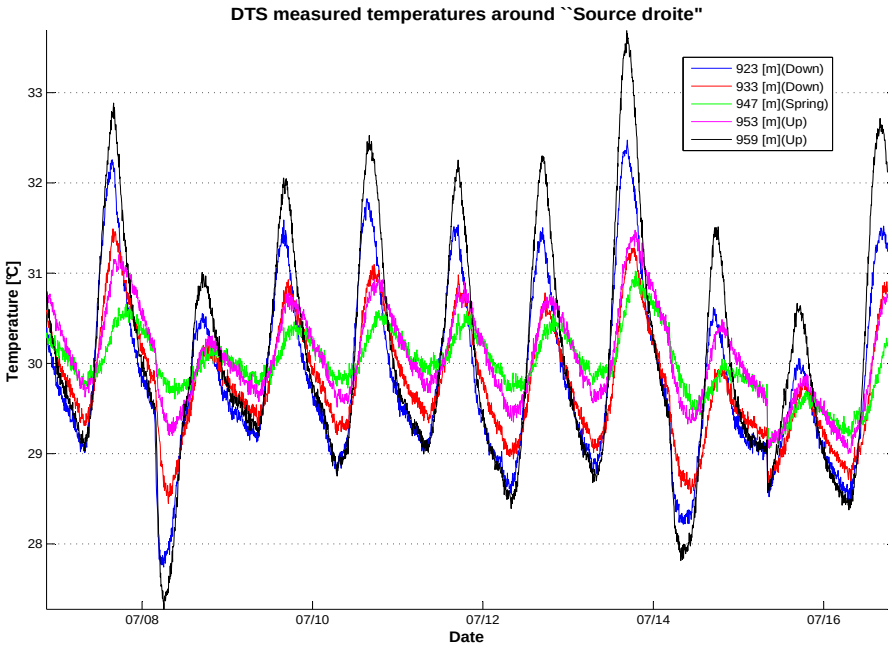

Figure 7.2: **Temperature of the inflow at "Source droite"**

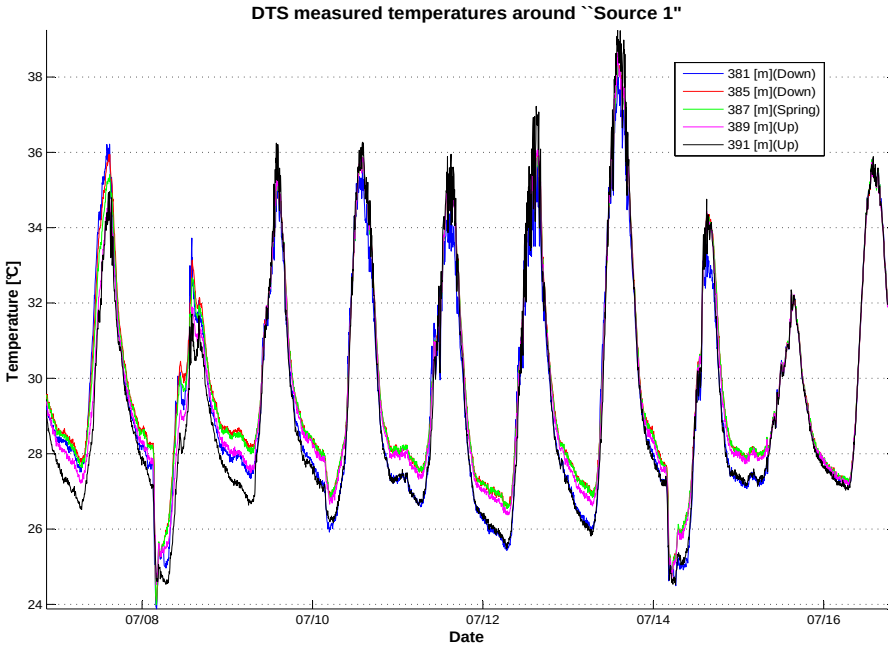

Figure 7.3: **Temperature of the inflow at "Source 1"**

fluctuates a lot. We can not confirm here that groundwater is flowing into the stream at this place! However, the red line shows a constant temperature at night around 28 °C. Some more measurements in this area of the discharge variation and temperature at different soil depth, would precise the nature of this spring.

Summary

To consider a single station dataset representative of the whole basin is not completely wrong as confirmed by the results of the model and the figures above. However, as soon as we want to increase the model accuracy, differences should be taken into account. The upstream part of the river, in the canyon, should be modeled with the data from station 1015 and the rest can be modeled like it has been done in this study with station 1000.

The spring location of spring "Source droite" is easy to recognize. The model accounts for it and the temperatures between the model and the reality are not so different. The spring "Source 1" (downstream) is more difficult to recognize and its temperature does not allow to determine whether it comes from the groundwater or from a subsurface flow. Some more study should be done at this location for further clarification.

The too large cooling effect in the upstream area of the model can be due to the simplification of using a single station for the input parameters. Long wave radiation is the main reason for cooling down the stream water. The effects of the surrounding rocks could increase the radiation from the landscape, controlled in the model with the parameter, θ_{VTS}.

Chapter 8

Conclusion and model improvements

DTS optical fiber data are providing a very good knowledge of main thermodynamic processes along the river, but inherent "noise" can lead to false interpretations. Coupling DTS optical fiber measurement to a stream water temperature model helps interpreting these irregularities. Not only, it allows to better understand the physical processes governing the energy fluxes acting on the stream, it can also help quantifying the discharges flowing into the stream.

The high temperature resolution presents advantages but also disadvantages. On one hand, it allows to determine thermal regimes along the river with great accuracy. A spring has a different thermal signature than a groundwater inflow or than a subsurface flow. On the other hand, the high resolution at local scale makes interpretation difficult in a system in equilibrium because of water mixing, soil heat conduction and air-water heat exchanges. A larger amount of measurements in the vicinity (15-100 [cm] away) of the river would complete DTS dataset.

Building the model on meteorologic data gives an overall control of the stream temperature dynamics. Namely, in this study, we could illustrate the fact that a continuous decreasing subsurface flow lead to warming of the river for some days after a rain event. We also could see that during night, the temperature decreases from upstream to downstream and this is not the result of groundwater inflow. During the day, when solar radiation is warming the river, the temperature increases from upstream to downstream. This is the result of the positive energy balance acting on the river at that time.

Another setup of stream temperature measurement could also be done to increase the knowledge of groundwater influence on stream thermal regime. Hatch et al. in 2006 [12] have measured stream bed temperatures at different depth and at different locations along a stream in Nevada (USA). The temperature daily gradient series within the stream bed can give reliable information about groundwater fluxes into the river or leaving the river. This can be done using Tidbit temperature loggers or also the DTS optical fiber. This latter can be buried at different depths inside the stream bed, hopefully, without disturbing too much its structure. However, as we do not know the real depth of burial at all times of measurements, coupling both techniques can be useful.

The modeling scale in time and in space are small. The regions are diverse (forest, riparian, steep valley) and the relevant parameters of each reach of the river cannot be compared to similar environments in other places. Roth et al., 2010 [18] show that the effects of vegetation on stream water temperature can be estimated with a physically based stream temperature model.

Bibliography

[1] Bradbury Kenneth R. and Xu Yongxin, **Foreword to special section: Groundwater in Africa**, Published in Ground Water vol. 48 (2010) (pp. 227-238)

[2] Brutsaert Wilfried, **Evaporation into the atmosphere**, London: England (1982)

[3] Cooperation@EPFL, Info4Dourou project, http://cooperation.epfl.ch/page68433.html

[4] Cadbury S. L., Hannah D. M. et al., **Stream temperature dynamics within a New-Zealand glacierized river basin**, Published in River research and applications, University of Leeds, England (2008)

[5] Connant Brewster Jr, **Delineating and quantifying ground water dioscharge zones using streambed temperatures**, Published in Ground water vol. 42 (2004) (pp. 243-257)

[6] Constantz Jim, Thomas Carole L. et al., **Influence of diurnal variations in stream temperature on streamflow loss and groundwater recharge**, Water resources research, Vol. 30, (1994) (pp. 3253-3264)

[7] Courtois Natalie et al., **Large-Scale Mapping of Hard-Rock Aquifer Properties Applied to Burkina Faso**, Published in Ground Water vol. 48 (2010) (pp. 269-283)

[8] EFLUM, Gallery, http://eflum.epfl.ch/gallery

[9] EPFL, Climatic instruments sensors, http://sensorscope.epfl.ch/climaps

[10] EPFL, Climatic instruments sensors details, http://sensorscope.epfl.ch/index.php/$Main_Page$

[11] EPFL, Info4Dourou database 2009

[12] Hatch Christine E., Fisher Adrew T. et al., **Quantifying surface water-groundwater interactions using time series analysis of streambed thermal records: method development**, Published Water Resour. Res., Vol. 42 (2006)

[13] Matthey Malik, Rapport de stage Master au Burkina Faso (Sep. 2009), http://cooperation.epfl.ch/webdav/site/cooperation/shared/Info4Dourou/Stage Master EPFL 2009 Malick.pdf

[14] Mays Larry W., **Water resources engineering**, 2005 Edition, pp 89-94

[15] Musy André, Soutter Marc, **Physique du sol Vol. 6**, Collection Gérer l'environnement, 1991, ISBN 2-88074-211-0, pp 87-92

[16] Neilson Bethany T., Hatch Christine E. et al., **Solar Radiative Heating of Fiber Optic Cables Used to Monitor Temperatures in Water** *Water Resour. Res.*, doi:10.1029/2009WR008354, in press.(accepted 19 April 2010)

[17] Ochsner Tyson E., Sauer Thomas J. et al., **Soil heat storage measurements in energy balance studies**, Published by American society of Agronomy (1992)

[18] Roth T.R., Westhoff Martjin C. et al., **Stream Temperature Response to Three Riparian Vegetation Scenarios by Use of a Distributed Temperature Validated Model**, Published in Environ. Sci. Technol., Vol. 44 (6) (2010) (pp 2072-2078)

[19] Selker J. S. et al., **Fiber optics opens window on stream dynamics**, Published in Geophys. Res. Lett. 33, (2006b)

[20] Temperature measurement technology, http://www.envco.co.nz/files/MO-ON-UTBI-001-L.jpg

[21] Tyler Scott W., **Distributed Temperature Sensing using Fiber Optics**, University of Nevada, Reno Dept. of Geologic Sciences and Engineering, website: $http://www.nvwra.org/annual_conf/2007/docs/nwrav2_tyler.pdf$

[22] U.S Environmental Protection Agency, **Molalla-Pudding Subbasin (appendix C)**, Oregon (December 2008)

[23] Water balance image, http://www.rfi.fr/actufr/images/077/eau430.jpg

[24] Westhoff Martjin C. et al., **A distributed stream temperature model using high resolution temperature observations**, Published in Hydrol. Earth Syst. Sci. Discuss. (2007)